

# Comparison of Atmospheric Parameters Determined from Spectroscopy and Photometry for DA White Dwarfs in the Sloan Digital Sky Survey

C. Genest-Beaulieu, & P. Bergeron

*Département de Physique, Université de Montréal, C.P. 6128, Succ. Centre-Ville, Montréal, QC H3C 3J7, Canada; genest@astro.umontreal.ca, bergeron@astro.umontreal.ca*

## ABSTRACT

We present a comparative analysis of atmospheric parameters obtained with the so-called photometric and spectroscopic techniques. Photometric and spectroscopic data for 1360 DA white dwarfs from the Sloan Digital Sky Survey (SDSS) are used, as well as spectroscopic data from the Villanova White Dwarf Catalog. We first test the calibration of the *ugriz* photometric system by using model atmosphere fits to observed data. Our photometric analysis indicates that the *ugriz* photometry appears well calibrated when the SDSS to AB<sub>95</sub> zeropoint corrections are applied. The spectroscopic analysis of the same data set reveals that the so-called high- $\log g$  problem can be solved by applying published correction functions that take into account 3D hydrodynamical effects. However, a comparison between the SDSS and the White Dwarf Catalog spectra also suggests that the SDSS spectra still suffer from a small calibration problem. We then compare the atmospheric parameters obtained from both fitting techniques and show that the photometric temperatures are systematically lower than those obtained from spectroscopic data. This systematic offset may be linked to the hydrogen line profiles used in the model atmospheres. We finally present the results of an analysis aimed at measuring surface gravities using photometric data only.

*Subject headings:* stars: fundamental parameters — techniques: photometric — techniques: spectroscopic — white dwarfs

## 1. Introduction

Various methods have been developed over the years to measure the atmospheric parameters — effective temperature ( $T_{\text{eff}}$ ) and surface gravity ( $\log g$ ) — of hydrogen-line DA white

dwarfs (see Bergeron et al. 1992 for a review). By far, the most commonly employed method nowadays is the so-called spectroscopic technique, where the profiles of the hydrogen Balmer lines are compared with the predictions of detailed model atmospheres (Bergeron et al. 1992, Vennes et al. 1997, Liebert et al. 2005, Koester et al. 2009b, Tremblay et al. 2011a, Gianninas et al. 2011, to name a few). A similar approach can of course be applied to any type of white dwarfs, such as DB stars (Voss et al. 2007; Bergeron et al. 2011). When the spectroscopic lines vanish at low effective temperatures, however, one must rely on the spectral energy distribution obtained from broad band energy distributions, and apply the photometric technique where measured magnitudes in various passbands are converted into average fluxes and compared to predicted fluxes from model atmospheres. Such a technique has been successfully applied in the context of cool white dwarfs by Bergeron et al. (1997, 2001), for example, using optical *BVRI* and infrared *JHK* photometry, or by Kilic et al. (2010) using *ugriz* photometry in the optical instead. In such cases, the effective temperature can be measured directly, but the surface gravity can only be determined if the distance to the star is known through parallax measurements for instance (Bergeron et al. 2001). Both the photometric and spectroscopic techniques are powerful methods since they can be applied routinely to large samples of white dwarfs.

Because of the sensitivity of the Balmer lines to variations in both  $T_{\text{eff}}$  and  $\log g$ , the *precision*<sup>1</sup> of the spectroscopic technique is extremely high, in particular in the context of DA stars. Indeed, Liebert et al. (2005) have determined, using multiple spectroscopic measurements of the same stars, that the precision could be as high as 1.2% in  $T_{\text{eff}}$  and 0.038 dex in  $\log g$ . While the spectroscopic technique is arguably the most precise method for measuring atmospheric parameters of white dwarf stars, it also depends heavily on the details of the physics of line broadening, and the calculations of atomic level populations. For instance, the improved Stark profiles of Tremblay & Bergeron (2009), which include nonideal effects directly into the line profile calculations, can yield differences as high as 1000 K in  $T_{\text{eff}}$  and 0.1 dex in  $\log g$ , which are even larger than the quoted precision of the spectroscopic technique! Even more dramatic are the effects of 3D hydrodynamical calculations on the predicted line profiles, compared to standard model atmospheres calculated within the mixing-length theory (see Tremblay et al. 2013 and references therein). So even though the spectroscopic technique has a high degree of precision, it may still lack a similar level of accuracy.

While the photometric technique is admittedly less precise than the spectroscopic method, it has the definite advantage of being less sensitive to the details of model atmosphere calculations since it relies mostly on the emergent continuum fluxes. On the other hand, the

---

<sup>1</sup>For completeness, the precision of a measurement refers to its reproducibility or repeatability, while the accuracy is related to the closeness of the measured parameter to its actual true value.

photometric technique depends heavily on the flux calibration used to convert observed magnitudes into observed average fluxes, as discussed at length by Holberg & Bergeron (2006). Ideally, one would like to compare both the spectroscopic and photometric techniques for a large ensemble of spectroscopic and photometric data for the same objects.

The large number of white dwarf stars identified in the Sloan Digital Sky Survey (SDSS) offers such a unique opportunity to compare atmospheric parameters derived from photometry, using the homogeneous set of *ugriz* photometric data, and from spectroscopy, using the homogeneous set of medium resolution spectroscopic data, which are available *for the same objects*. Such a comparison has been performed by Tremblay et al. (2013, see their Figure 16) but only for a limited range of effective temperatures. Note also that Eisenstein et al. (2006) used both photometric and spectroscopic data simultaneously to measure the atmospheric parameters of the white dwarfs in the Data Release 4. Because we are interested here in comparing the results from both techniques, and in particular the temperature scales, we will consider these two data sets independently.

We thus present in this paper a detailed comparison of the photometric and spectroscopic techniques applied to the DA stars identified in the SDSS. The photometric sample used in our sample is described and analyzed in Section 2, where we also explore the effects of interstellar reddening and other issues related to flux calibration. The optical spectra for the same objects are then analyzed in Section 3, together with independent white dwarf spectra drawn from the Villanova White Dwarf Catalog, which are used to test the flux calibration of the SDSS spectroscopic data. The effective temperatures derived from both photometric and spectroscopic techniques are then compared in Section 4, while in Section 5, we exploit the sensitivity of the  $u - g$  color index to  $\log g$  to compare surface gravities measured photometrically and spectroscopically. Our summary and conclusions follow in Section 6.

## 2. Photometric Analysis

### 2.1. Photometric Sample

Our photometric sample is based on the Data Release 7 (DR7) of the Sloan Digital Sky Survey (Kleinman et al. 2013), which contains 19,713 white dwarfs of various spectral types, including 12,831 DA stars. We exclude from this sample all subtypes DAB, DAO, etc. Since the main purpose of our analysis is to compare atmospheric parameters derived from photometry and spectroscopy, we retain only the best data sets for each technique, and we thus restrict our photometric sample to white dwarfs with a signal-to-noise ratio above 25

in the  $g$ -band, and with uncertainties less than 0.1 mag in all bandpasses. Applying these criteria, we end up with a sample of 1478 *ugriz* photometric data sets for 1360 DA white dwarfs, given that some objects have been observed more than once. Those are treated as independent observations.

Our photometric sample is summarized in the  $(u - g, g - r)$  two-color diagram displayed in Figure 1. Also superimposed on the observations are the theoretical photometric sequences for hydrogen atmosphere white dwarfs from Holberg & Bergeron (2006)<sup>2</sup>. Note that the magnitudes displayed here have been corrected for interstellar reddening following a procedure described in Section 2.6. One can already notice the sensitivity of the  $u - g$  color index to surface gravity between  $T_{\text{eff}} \sim 8000$  K and 17,000 K, which measures the strength of the Balmer jump resulting from a competition between bound-free atomic hydrogen and free-free  $\text{H}^-$  opacities (see Weidemann 1971, Shipman & Sass 1980). We will attempt later to exploit this particular sensitivity to  $\log g$  (see Section 5).

## 2.2. Photometric Technique

Atmospheric parameters,  $T_{\text{eff}}$  and  $\log g$ , of white dwarf stars can be measured with the photometric technique described in Bergeron et al. (1997), where photometric measurements are converted into spectral energy distributions, which are then compared with those predicted from model atmosphere calculations. Although usually applied in the context of cool degenerates when the optical spectra become almost completely featureless, we will apply this method to all objects in our sample and will attempt to evaluate its validity over the entire temperature range covered by the SDSS. In the case of the SDSS *ugriz* photometry, the magnitude system is defined in terms of  $\text{AB}_{95}$  magnitudes, where we apply a correction to the  $u$ ,  $i$ , and  $z$  bands of  $-0.040$ ,  $+0.015$ , and  $+0.030$ , respectively, to account for the transformation from the SDSS to the  $\text{AB}_{95}$  magnitude system, as explained in Eisenstein et al. (2006). We first transform every magnitude  $m_\nu$  into an average flux  $f_\nu^m$  using the equation

$$m_\nu = -2.5 \log f_\nu^m - 48.60, \quad (1)$$

where

$$f_\nu^m = \frac{\int f_\nu S_m(\nu) d \log \nu}{\int S_m(\nu) d \log \nu}, \quad (2)$$

---

<sup>2</sup>See also <http://www.astro.umontreal.ca/~bergeron/CoolingModels>.

and where  $f_\nu$  is the monochromatic flux from the star received at Earth, and  $S_m(\nu)$  is the total system response including the atmospheric transmission corresponding to an air mass of 1.3 and mirror reflectance, as well as the detector quantum efficiency (Holberg & Bergeron 2006). A set of transmission curves for the SDSS filters measured by Jim Gunn in 2001 is available on the survey’s website<sup>3</sup>. A more recent estimate of these curves has been published by Doi et al. (2010), and this will be the set of transmission curves used here; a comparison of the photometric temperatures obtained with these two sets of filters is presented in Section 2.4.1. Since the observed fluxes correspond to averages over given bandpasses, the monochromatic fluxes from the model atmospheres need to be converted into average fluxes as well,  $H_\nu^m$ , which can be done by substituting  $f_\nu$  in Equation 2 with the monochromatic Eddington flux  $H_\nu$ . We can then relate the average observed fluxes  $f_\nu^m$  and the average model fluxes  $H_\nu^m$  — which depend on  $T_{\text{eff}}$  and  $\log g$  — by the equation

$$f_\nu^m = 4\pi(R/D)^2 H_\nu^m \quad (3)$$

where  $R/D$  defines the ratio of the radius of the star to its distance from Earth. In the above equation, the radius  $R$  is obtained from the  $\log g$  value by using evolutionary models similar to those described in Fontaine et al. (2001) but with C/O cores,  $q(\text{He}) \equiv \log M_{\text{He}}/M_\star = 10^{-2}$ , and  $q(\text{H}) = 10^{-4}$ , which are representative of hydrogen-atmosphere white dwarfs. We then minimize the  $\chi^2$  value defined in terms of the difference between observed and model fluxes over all bandpasses, properly weighted by the photometric uncertainties. Our minimization procedure relies on the nonlinear least-squares method of Levenberg-Marquardt (Press et al. 1986), which is based on a steepest decent method. In principle, for stars with known trigonometric parallax measurements, the distance  $D$  in Equation 3 can be obtained directly, in which case the minimization procedure yields the effective temperature and the radius of the star. However, for all white dwarfs in the SDSS, for which parallaxes are not available, we will simply assume a value of  $\log g = 8.0$ , although we will also experiment with spectroscopic  $\log g$  values (see Section 2.4.3). In these cases,  $T_{\text{eff}}$  and the solid angle  $\pi(R/D)^2$  are considered free parameters, and the uncertainties of both parameters are obtained directly from the covariance matrix of the fit.

To measure the atmospheric parameters from photometry, we rely on two different sets of model atmospheres and synthetic spectra. For effective temperatures below 30,000 K, synthetic spectra are calculated using the LTE approximation and the ML2/ $\alpha=0.7$  version of the mixing-length theory to treat the atmospheric convection, which becomes important below  $T_{\text{eff}} = 15,000$  K, using the model atmosphere code described at length

---

<sup>3</sup><http://www.sdss3.org/instruments/camera.php>

in Tremblay & Bergeron (2009) and references therein. For  $T_{\text{eff}} > 30,000$  K, NLTE effects are taken into account using TLUSTY (Hubeny & Lanz 1995). Combining these two grids, we obtain model spectra for effective temperatures ranging from  $T_{\text{eff}} = 1500$  K to  $T_{\text{eff}} = 120,000$  K and for surface gravities between  $6.0 \leq \log g \leq 9.5$ . These models also include the improved Stark broadening profiles from Tremblay & Bergeron (2009).

### 2.3. Selection of the Sample

Since our goal is to compare the atmospheric parameters obtained from photometric and spectroscopic data, we want to retain only the best data available for each set. It was mentioned earlier that the photometric sample was limited to DA white dwarfs with a signal-to-noise ratio above 25 in the  $g$  band and  $\sigma_{m\nu} < 0.1$  in all bandpasses (see Section 2.1). These criteria alone are not sufficient to eliminate all bad data from our sample, however, as illustrated in Figure 2 where we show representative photometric fits as a function of increasing reduced  $\chi^2$  values (i.e., divided by number of degrees of freedom). While the fits displayed in the left panels are excellent, those in the right panels are more problematic. Since the photometric technique is based on a  $\chi^2$  minimization approach, we can use these results to define a critical value  $\chi_{\text{crit}}^2$  above which the  $ugriz$  data are considered unreliable and are excluded from our photometric sample.

Figure 3 shows the reduced  $\chi^2$  distribution obtained from our fits using the photometric technique. This distribution reveals that for most of the objects, the photometric energy distributions are well reproduced (low  $\chi^2$  values). However, for several stars, the observed magnitudes cannot be fitted properly by the photometric technique (high  $\chi^2$  values). Since we do not want to consider these objects in our comparative analysis, we define a value for  $\chi_{\text{crit}}^2$  above which the photometric fits will not be considered accurate enough for our purposes. By examining the results of our photometric fits and corresponding  $\chi^2$  values, we have arbitrarily determined that by setting  $\chi_{\text{crit}}^2 = 3$ , most bad fits were successfully excluded from the sample. According to this criterion, all fits displayed in the right panels of Figure 2 would be excluded.

This additional reduced  $\chi^2$  criterion ensures that we now have a clean photometric sample. In some cases, however, this criterion may lead to the exclusion of good data sets. Indeed, since we assumed  $\log g = 8.0$  for all objects in our sample, white dwarfs with effective temperatures between  $T_{\text{eff}} \sim 8000$  K and  $\sim 17,000$  K, for which the  $u - g$  color index is sensitive to surface gravity (see Figure 1), may be excluded from our sample if their  $\log g$  value differs significantly from 8.0. For instance, the object 042017.86+052735.8 displayed in Figure 2 has a *spectroscopic*  $\log g$  value of 8.362, and forcing  $\log g = 8.0$  thus leads to

a bad photometric fit and corresponding large value of  $\chi_{\text{red}}^2 \sim 10$ . One solution to this problem would be to use only the *griz* photometry, thus avoiding the *u* bandpass which is  $\log g$  sensitive. However, as discussed in Section 2.4, the *u*-band photometry is important for the analysis of hot white dwarfs ( $T_{\text{eff}} \gtrsim 20,000$  K), and we want to use a consistent approach for all stars, regardless of their effective temperature. Another solution would be to rely on spectroscopic  $\log g$  values since all white dwarfs in our photometric sample have a measured SDSS spectrum. But since the goal of our study is to compare the atmospheric parameters measured *independently* from the photometric and spectroscopic techniques, we prefer to assume  $\log g = 8.0$  throughout. Considering these facts, we will retain all objects in our analysis, but will display those with  $\chi_{\text{red}}^2 > \chi_{\text{crit}}^2$  with a different color symbol.

## 2.4. Selected Results

### 2.4.1. Transmission Curves

The SDSS filters were designed to collect fluxes in the ultraviolet (*u*), green (*g*), red (*r*), near-infrared (*i*), and far infrared (*z*). For the *g*, *r*, and *i* filters, the red wavelength cutoff is achieved by applying an interference coating. These layers dehydrated when they were placed in the vacuum of the camera, changing the refractive index of the interference coating. The dehydration caused the red edges of these three filters to be shifted blueward (Fan et al. 2001). However, it seems the *u* filter was the one that has changed the most with time (Doi et al. 2010). The *u* filter has a natural red leak around  $7100 \text{ \AA}^4$ , which is usually suppressed by the application of an interference coating. The refractive index of this interference coating also changed due to dehydration when the filter was placed in the vacuum of the camera, so the natural red leak is not completely suppressed. We explore the effects of this red leak on the results of the photometric temperatures in Section 2.4.2.

It was mentioned in Section 2.2 that there are two sets of transmission curves for the *ugriz* filters. The first one, measured by Jim Gunn in 2001, is available on the SDSS website. It is important to point out that these filter curves do not include the complete system response from atmosphere to detector<sup>5</sup>. A more recent estimate of these transmission curves, using more data points and a larger time baseline, was published in Doi et al. (2010). Both sets of transmission curves are shown in Figure 4; note that each curve has been normalized to unity for easier comparison. Since the curves measured by Gunn in 2001 were used in

---

<sup>4</sup><http://cas.sdss.org/dr7/en/help/docs/algorithm.asp?key=photometry>

<sup>5</sup><http://www.sdss3.org/instruments/camera.php>

several investigations prior to the publication of Doi et al., we wanted to evaluate the effect of the filter transmission curves on the photometric results. Figure 5 presents a comparison of effective temperatures obtained using both sets of transmission curves. The results clearly show that the photometric results are not affected by the particular choice of transmission curves. Since the Doi et al. curves are more recent and use more data points, we will use those in the remainder of our analysis.

#### 2.4.2. The *u*-band

As mentioned above, the *u* filter has a natural red leak around 6000-8000 Å, which is supposed to be suppressed by an interference coating (Doi et al. 2010). The dehydration of this coating shifted the wavelength cutoff blueward, thus the problem is only partially corrected and a small leak still remains near 7700 Å. Since we want to compare atmospheric parameters determined from photometry and spectroscopy, we have to make sure that the *u*-band red leak does not affect the results of the photometric technique. To achieve this, we can compare effective temperatures obtained from *ugriz* photometry with those obtained by ignoring the *u*-band photometry. These results are shown in Figure 6.

Cooler stars have an important flux contribution in the red region of the electromagnetic spectrum, and the red leak could potentially affect their photometric temperatures more significantly. But as shown in Figure 6, the effective temperatures obtained using *ugriz* or only *griz* are very similar for  $T_{\text{eff}} < 20,000$  K. This suggests that the red leak does not affect the photometric results significantly for cool white dwarfs. At higher temperatures, however, the scatter in the distribution becomes more important. Since hot white dwarfs emit very little flux in the red portion of the electromagnetic spectrum, it is unlikely that the scatter has anything to do with the *u* filter red leak. A more likely explanation is that any photometry in the optical becomes less sensitive to  $T_{\text{eff}}$  for hotter stars, as the energy distribution falls into the Rayleigh-Jeans regime, and one needs to push the photometry further into the ultraviolet. Hence the increased scatter observed in Figure 6 above  $T_{\text{eff}} \sim 20,000$  K is certainly due to larger uncertainties in photometric temperatures based on *griz* photometry only, and not to the *u*-band red leak, and these results stress the importance of including *u*-band photometry to estimate the effective temperature of hotter white dwarfs.



### 2.4.3. Effects of the Surface Gravity

Since no parallax measurement is available for any of the SDSS white dwarfs in our sample, we simply assume a value of  $\log g = 8.0$  to estimate the photometric temperatures. However, since surface gravities for white dwarfs are found in a wide range of values,  $6.5 \lesssim \log g \lesssim 9.5$ , our assumption of  $\log g = 8.0$  could have an effect on the photometric temperatures, especially in the range  $8000 \text{ K} < T_{\text{eff}} < 17,000 \text{ K}$  where the Balmer jump is sensitive to surface gravity (see Figure 1). As all white dwarfs in our photometric sample have been spectroscopically identified in the SDSS, they also have a measured spectrum. Therefore, we can apply the spectroscopic technique (see Section 3.2) to measure their surface gravities (properly corrected for 3D hydrodynamical effects — see Section 3.3), and then use these spectroscopic  $\log g$  values when fitting the photometry. We can then compare the corresponding photometric temperatures with those obtained under the assumption of  $\log g = 8.0$ . The results of this experiment are displayed in Figure 7.

Our results indicate that the assumption of  $\log g = 8.0$  does not affect the photometric temperatures significantly, even in the region where the  $u - g$  color index is particularly sensitive to surface gravity ( $8000 \text{ K} < T_{\text{eff}} < 17,000 \text{ K}$ ). This might be a surprising result at first given the strong  $\log g$  dependence illustrated in Figure 1 in this temperature range. And indeed, the photometric temperature of a  $T_{\text{eff}} = 14,700 \text{ K}$  object at  $\log g = 8.0$  drops to  $14,000 \text{ K}$  if we assume a value of  $\log g = 8.5$  instead, i.e. a  $700 \text{ K}$  temperature difference. However, a closer inspection of the results shown in Figure 7 between  $9000 \text{ K}$  and  $17,000 \text{ K}$  reveals that most temperature differences lie well within  $500 \text{ K}$ , and that only 5 objects exceed this value, mainly because the surface gravity distribution is so strongly peaked around  $\log g = 8.0$  ( $\sigma_{\log g} \sim 0.2$  in this temperature range; see Figure 14 below). Actually, one of these 5 objects is *042017.86+052735.8*, already discussed above (see Figure 2), with a spectroscopic value of  $\log g = 8.362$  significantly above average. This indicates that it would be more accurate to rely on spectroscopic  $\log g$  values, but again, since our goal is to compare the temperatures derived independently from the photometric and spectroscopic techniques, we will assume  $\log g = 8.0$  for the remainder of this analysis.

## 2.5. Photometric Calibration

Our next step is to ensure that the *ugriz* photometry is properly calibrated. It is well known that the *ugriz* photometric system is not entirely consistent with the  $\text{AB}_{95}$  system, and that small zeropoint offsets exist. These offsets in the  $u$ ,  $i$ , and  $z$  bands can be compensated by applying the appropriate corrections from Eisenstein et al. (2006), as discussed in Section 2.2. In this section, we attempt to validate the overall calibration of the *ugriz*

photometric system. One way to achieve this goal was presented by Holberg & Bergeron (2006) where the standard star Vega and four fundamental HST white dwarfs were used to test the calibration of the *UBVRI*, Strömgren, 2MASS, and *ugriz* photometric systems. By combining the measured spectrum and the proper set of transmission curves, they obtained computed magnitudes for each system, which were then compared to the observed photometry. The comparison was also extended to a set of 107 DA stars with *ugriz* photometry and spectroscopic values of  $T_{\text{eff}}$  and  $\log g$  available (see their Table 14). A disadvantage of this approach is that it relies on spectroscopic data as well as on the spectroscopic technique, while we would prefer a method that is completely independent from spectroscopy. We thus propose below a different method.

The photometric technique discussed above relies on a  $\chi^2$  minimization procedure to find the model energy distribution that best reproduces the observed photometry. We can therefore compare the *differences* between the observed *ugriz* data and the theoretical energy distribution predicted by the photometric technique. To avoid any bias, we do not restrain the sample to objects for which  $\chi_{\text{red}}^2 < \chi_{\text{crit}}^2$ . We do, however, consider only objects with  $T_{\text{eff}} \leq 20,000$  K since the photometric technique becomes less sensitive to temperature above this range; we also apply the SDSS to AB<sub>95</sub> zeropoint corrections from Eisenstein et al. (2006). The results for our photometric sample are displayed in Figure 8, where we show histogram distributions between observed (obs) and theoretical (th) magnitudes for each individual bandpass of the *ugriz* system. Our results show that all histograms appear symmetrical and well centered on  $m_{\nu,\text{obs}} - m_{\nu,\text{th}} = 0.0$ , which indicate that the *ugriz* photometric system is properly calibrated, at least in a relative sense. Indeed, if the *g* photometry, say, was not well calibrated, it would be systematically lower (or larger) than the predicted photometry, and the corresponding histogram would not be centered. Since the photometric technique fits the complete energy distribution, and not each photometric point individually, the *u* and *r* distributions would be shifted as well, but in the opposite direction. This is nicely illustrated in Figure 9, where the SDSS to AB<sub>95</sub> corrections have not been applied. Except for the *i*-band, all histograms are not centered, a result that demonstrates the necessity to apply these zeropoint corrections.

Despite these reassuring results, there could still be a calibration issue that depends on the observed magnitude. For example, if  $m_{\nu,\text{obs}} > m_{\nu,\text{th}}$  for bright objects and  $m_{\nu,\text{obs}} < m_{\nu,\text{th}}$  for faint objects, the histograms displayed above would still be centered on average. To investigate this possibility, we illustrate in Figure 10 the same magnitude differences,  $m_{\nu,\text{obs}} - m_{\nu,\text{th}}$ , but this time as a function of the observed magnitude. As can be seen, all distributions are centered regardless of the magnitude. Moreover, except for the *z*-band, the scatter in the distributions remains somewhat constant with the observed magnitude. For the *z*-band, the dispersion becomes more important with larger  $z_{\text{obs}}$ . This can also be

observed in the histograms from Figure 8 where  $\sigma_z = 0.041$ , while  $\sigma_{m_\nu} \sim 0.02 - 0.03$  for the other bands. The dispersion affects mostly objects that are very faint in the mid-infrared region ( $z > 18.0$ ). Since the SDSS camera images  $1.5 \text{ deg}^2$  at once, the exposure time is the same for every object and this might not be sufficient enough to ensure a good signal-to-noise ratio in the  $z$ -band. This is also reflected in the photometric uncertainties, where we obtain an average of  $\langle\sigma_z\rangle = 0.031$  for the overall sample, compared to  $\sim 0.02$  for the other bands.

In the same context, we would like to point out that the mean uncertainties for each photometric band —  $\langle\sigma_u\rangle = 0.021$ ,  $\langle\sigma_g\rangle = 0.019$ ,  $\langle\sigma_r\rangle = 0.016$ ,  $\langle\sigma_i\rangle = 0.018$ , and  $\langle\sigma_z\rangle = 0.031$  — are somewhat smaller than the standard deviations of the distributions observed in Figure 8 —  $\sigma_u = 0.032$ ,  $\sigma_g = 0.027$ ,  $\sigma_r = 0.018$ ,  $\sigma_i = 0.022$ ,  $\sigma_z = 0.041$ , which suggests that the quoted photometric uncertainties of the *ugriz* data might be slightly underestimated.

## 2.6. Interstellar Reddening

Due to the nature of the Sloan Digital Sky Survey, white dwarf stars in our photometric sample are particularly faint ( $16 < g < 20$ ) — see Figure 10. Consequently, some white dwarfs in this sample may be quite distant, and their magnitudes are thus likely to be affected by interstellar reddening. We can estimate the distance to each star in our sample by using the photometric technique, which yields the value of the solid angle  $\pi(R/D)^2$ , and thus the distance  $D$  for a stellar radius  $R$  corresponding to our assumed value of  $\log g = 8$  at the photometric temperature (derived from our evolutionary models). Since this assumption on  $\log g$  directly affects our distances, we can improve upon these estimates by relying instead on the spectroscopic  $\log g$  values described in the next section. These *photometric distances* for our SDSS sample are shown in Figure 11. As this figure shows, many stars in this sample are indeed found at large distances ( $> 100 \text{ pc}$ ), implying that their magnitudes are most likely affected by interstellar extinction. We thus modified our photometric technique to deredden the observed magnitudes. Our procedure is identical to that described in Tremblay et al. (2011a), based on the parameterization of Harris et al. (2006) for the amount of reddening as a function of distance. This procedure works in an iterative fashion, using the distance of the star found from the previous iteration. Interstellar absorption is assumed to be negligible for stars with distances less than  $100 \text{ pc}$ , and maximum for stars with distances  $|z| > 250 \text{ pc}$  from the Galactic plane. The absorption is assumed to vary linearly along the line of sight between these two regimes.

Figure 12 compares the effective temperatures obtained from underreddened and dereddened *ugriz* magnitudes. As expected, temperatures obtained from dereddened magnitudes are systematically higher than those measured with underreddened photometry. The effect of

interstellar reddening is particularly important for hotter stars ( $T_{\text{eff}} > 12,000$  K). Since most stars in the SDSS are faint, the hotter white dwarfs, which are intrinsically more luminous, are likely to be more distant than their cooler siblings, and thus more affected by reddening. We also note in Figure 12 an increase in dispersion at higher temperatures, which probably reflects a spread in distances, and thus in the corresponding amount of reddening.

As Figure 12 clearly illustrates, the photometric temperatures are particularly sensitive to interstellar extinction, especially for hot white dwarfs, and all *ugriz* magnitudes will be dereddened in the remainder of our analysis, unless otherwise specified. We also keep in mind, however, that our procedure for taking into account the effects of interstellar reddening remains approximate.

### 3. Spectroscopic Analysis

#### 3.1. Spectroscopic Samples

Since the DR7 White Dwarf Catalog (Kleinman et al. 2013) contains only spectroscopically identified white dwarfs, all stars in our photometric sample also have a measured spectrum in the SDSS database. Therefore, our spectroscopic sample is composed of the same stars as the photometric sample. All spectra for this sample have been acquired from the SDSS Data Archive Server<sup>6</sup> (DAS), which contains the data up to DR7, inclusively. The spectra were reduced with the DR7 data reduction algorithm<sup>7</sup>; each spectrum has a spectral coverage from 3800 Å to 9200 Å with a resolution of 3 Å (FWHM).

We also use for comparison the spectroscopic sample from Gianninas et al. (2011). This sample contains 1150 bright ( $V \leq 17.5$ ) DA white dwarfs drawn from the online version of the Villanova White Dwarf Catalog of McCook & Sion (1999). These spectra have a high signal-to-noise ratio ( $S/N \sim 70$ ) and were acquired with different instruments over a time period of about 20 years, so the spectral coverage and spectral resolution differ from one spectrum to another (from 3 Å to 9 Å FWHM); for more information on data acquisition, see Section 2 of Gianninas et al. (2011).

---

<sup>6</sup><http://das.sdss.org/spectro/>

<sup>7</sup><http://www.sdss.org/dr7/algorithms/index.html>

### 3.2. Spectroscopic Technique

The best method for measuring the atmospheric parameters of DA stars using spectroscopic data was first discussed in detail by Bergeron et al. (1992). This so-called spectroscopic technique was then improved by Bergeron et al. (1995a), and more recently by Liebert et al. (2005). This technique allows us to determine the effective temperature and the surface gravity of a white dwarf by comparing its observed spectrum to a grid of model spectra. The first step is to normalize the flux from each individual line to a continuum set to unity at a fixed distance from the line center, for both observed and model spectra. Observed and synthetic spectra are then compared in terms of line shapes only. There are two approaches to define the spectrum continuum. The first one is used when the star’s effective temperature is in the interval  $9000 \text{ K} < T_{\text{eff}} < 16,000 \text{ K}$  where the Balmer lines are strong. The normalization is then performed using a sum of pseudo-gaussian profiles, which prove to be a good approximation for the observed Balmer lines. If the star lies outside of this temperature range, Balmer lines become weak and the continuum between those lines is essentially linear, therefore pseudo-gaussian profiles cannot be used as easily. We rely instead on model spectra to reproduce the overall spectrum. In this case, we include a wavelength shift and several order terms in  $\lambda$ , up to  $\lambda^6$ , using the nonlinear least-square method of Levenberg-Marquardt (Press et al. 1986). At this point, we have a smooth model fit, but the values of  $T_{\text{eff}}$  and  $\log g$  obtained in this manner are meaningless since too many fitting parameters are used. Now that every line is normalized, we can proceed to determine the values of  $T_{\text{eff}}$  and  $\log g$  using our grid of model spectra, convolved with the appropriate instrumental gaussian profile (3, 6, or 9 Å, depending on the resolution of the observed data), and the same fitting method. When the effective temperature of the white dwarf is close to the region where the equivalent widths of the Balmer lines reach their maximum ( $T_{\text{eff}} \sim 13,500 \text{ K}$ ) two solutions are possible, one on each side of the maximum. Here we take advantage of the available *ugriz* photometry and adopt the photometric temperature obtained previously as the starting point of this iterative process.

Sample fits using the spectroscopic technique are displayed in Figure 13. As illustrated here, some of the SDSS spectra in our sample were found to be problematic (see, e.g., bottom fits in Figure 13) and these have been removed from our sample.

### 3.3. 3D Hydrodynamical Corrections

Even though the spectroscopic technique is arguably the most *precise* technique for measuring the atmospheric parameters of DA stars,  $T_{\text{eff}}$  and  $\log g$ , we still need to determine whether the resulting parameters are also *accurate*. One way to accomplish this is to com-

pare the atmospheric parameter distributions with the predictions of evolutionary tracks at constant masses. Such a comparison for the SDSS and the Gianninas spectroscopic samples is shown in the top panels of Figures 14 and 15, respectively, together with a single mass evolutionary track corresponding to the median mass of each sample (see below).

In both distributions, it is obvious that surface gravities are overestimated at low effective temperatures ( $T_{\text{eff}} < 13,000$  K). This corresponds to the well documented high- $\log g$  problem (see, e.g., Tremblay et al. 2010 and references therein). Many scenarios have been proposed in the past to account for this problem, the most popular of which involves convective mixing. Since a hydrogen-atmosphere white dwarf becomes convective below  $T_{\text{eff}} \sim 15,000$  K, a significant amount of helium can be convectively mixed with the outer hydrogen atmosphere if the hydrogen layer is thin enough (Koester 1976; Vauclair & Reisse 1977; Dantona & Mazzitelli 1979). Helium would remain practically invisible at these temperatures, but the spectroscopic  $\log g$  values would appear higher than average when measured with pure hydrogen models (Bergeron et al. 1991). However, no trace of atmospheric helium has been reported in high dispersion, high S/N spectra (Tremblay et al. 2010), ruling out this scenario as a possible explanation for the high- $\log g$  problem. It is now commonly accepted that this overestimation is caused instead by the use of the mixing-length theory (MLT) to treat convective energy transport in 1D model atmospheres, and that the problem can be solved with the use of 3D hydrodynamical model atmospheres (Tremblay et al. 2011b). Tremblay et al. (2013) recently calculated a new grid of 3D model atmospheres and published correction functions (in both  $T_{\text{eff}}$  and  $\log g$ ) that can be applied to atmospheric parameters obtained from 1D/MLT models. These correction functions, reproduced here in Figure 16, indicate that below  $T_{\text{eff}} \sim 15,000$  K, i.e. when atmospheric convection becomes important, surface gravities obtained from 1D models are overestimated with respect to 3D models, and that the maximum corrections occur near  $\sim 10,000$  K regardless of the surface gravity of the star.

The atmospheric parameters for the SDSS and the Gianninas spectroscopic samples, corrected for 3D hydrodynamical effects, are shown in the bottom panels of Figures 14 and 15, respectively. The high  $\log g$  problem has now vanished, and both the SDSS and the Gianninas  $\log g$  distributions follow the evolutionary track well below  $T_{\text{eff}} \sim 13,000$  K. However, a closer inspection reveals that the atmospheric parameters for both samples are not fully corrected, and that surface gravities are still overestimated near  $T_{\text{eff}} \sim 12,000$  K. The cause of this slight overestimation is not fully understood, but Tremblay et al. (2013) suggest that this might be related to the opacity sources or the equation-of-state in the model atmospheres.

Another way to investigate the high- $\log g$  problem is to compare the mass distributions

of hot (radiative atmosphere) and cool (convective atmosphere) DA stars (unlike the surface gravity, the mass of a white dwarf remains constant with time). The mass distributions for white dwarfs in the SDSS and the Gianninas samples are displayed in Figures 17 and 18, respectively, for both the 1D/MLT models (left panels) and with the 3D corrections applied (right panels); the individual contributions for cool ( $T_{\text{eff}} < 13,000$  K) and hot ( $T_{\text{eff}} > 13,000$  K) white dwarfs are also shown. As observed in the left panels of these figures, the uncorrected mass distributions for hotter objects peak around  $M \sim 0.6 M_{\odot}$  for both samples, while they peak around  $M \sim 0.7 M_{\odot}$  for cooler objects. When the 3D corrections are applied, however, both distributions for hot and cool white dwarfs peak at  $M \sim 0.6 M_{\odot}$ . The mean mass of cool white dwarfs is still  $\sim 0.02 - 0.03 M_{\odot}$  larger than that of hotter objects, but this can probably be explained by the fact that the fraction of massive white dwarfs appears higher at low temperatures. We also notice that the mean mass of the Gianninas sample is about  $\sim 0.03 M_{\odot}$  larger than the SDSS sample, most likely due to a residual problem with the flux calibration of the SDSS spectroscopic data (see also Tremblay et al. 2011a, Gianninas et al. 2011, and next subsection).

### 3.4. Spectroscopic Calibration

As for the photometric sample, it is important to make sure that the spectroscopic data are properly calibrated. One way to accomplish this is to compare the behavior of the atmospheric parameter distributions (corrected for 3D hydrodynamical effects) for the SDSS and Gianninas samples, displayed in the bottom panels of Figures 14 and 15, respectively. A first discrepancy between these two distributions can be observed around  $T_{\text{eff}} \sim 14,000$  K where there is a small but significant accumulation of objects for the Gianninas sample, while there appears to be a small deficit for the SDSS sample in the same temperature range. This corresponds precisely to the temperature where the strength of the hydrogen Balmer lines reach their maximum. Since the spectroscopic technique relies on the strength of the hydrogen lines, such accumulations or gaps may appear in the temperature distributions if the lines in the model spectra are predicted too weak or too strong in this temperature range (see also Figure 3 of Bergeron et al. 1995b for a similar result). The fact that there is an accumulation of objects in that region for the Gianninas sample indicates that the models predict weaker lines than what is observed, while the opposite occurs for the SDSS sample. This difference in behavior suggests that at least one of our spectroscopic samples has a calibration issue.

Another discrepancy is visible when we compare both distributions to the evolution-ary tracks at a constant mass, as depicted in Figures 14 and 15. While the Gianninas

distribution follows the constant (median) mass evolutionary track through the entire temperature range displayed here, the surface gravities for the SDSS objects fall below the track above  $\sim 16,000$  K, and slightly above the track at lower temperatures, indicating that the SDSS spectroscopic sample may have a small calibration issue. This problem is well known and the SDSS data reduction algorithm has been improved several times to correct for this problem. A description of these improvements is available on the SDSS website<sup>8</sup>. The spectroscopic data used here have been reduced with the DR7 version of the algorithm described in Abazajian et al. (2009). It seems that, despite these improvements, the SDSS data reduction algorithm is still not perfect.

Finally, since the Gianninas spectroscopic sample covers more or less the entire sky, some of the white dwarfs lie in the SDSS field, and thus also have a measured SDSS spectrum. The method used to recover the spectra in common between both samples is described in the next section. Using this method, we identified 200 of the Gianninas white dwarfs that also have a measured spectrum in the SDSS. Figure 19 presents the comparison of effective temperatures obtained from the SDSS and the Gianninas spectroscopic data. For  $T_{\text{eff}} < 14,000$  K, SDSS spectra yield effective temperatures slightly lower than those obtained with the Gianninas spectra. For  $T_{\text{eff}} > 14,000$  K, however, the trend is more significant and in the opposite direction, with the SDSS temperatures being  $\sim 1100$  K higher, on average, than the Gianninas temperatures. Again, we believe that the SDSS spectroscopic data suffer from a small calibration problem, and we will keep this in mind when comparing spectroscopic and photometric temperatures.

#### 4. Comparison of Atmospheric Parameters

The goal of our study is to compare the atmospheric parameters (in particular the effective temperatures) obtained from photometric and spectroscopic observations. We will first consider the SDSS sample, for which *ugriz* photometry and optical spectroscopy are available for the same objects. We showed in Section 2.6 that white dwarfs in the SDSS are generally found at large distances, and thus that the observed magnitudes may be significantly affected by interstellar reddening. We also determined in Section 3.3 that 3D hydrodynamical corrections needed to be applied to the atmospheric parameters determined from the spectroscopic technique. In the remainder of our analysis, we thus systematically deredden the *ugriz* photometry following the procedure outlined in Section 2.6, and apply the 3D correction functions, unless otherwise specified.

---

<sup>8</sup><http://www.sdss.org/dr7/algorithms/dataProcessing.html>



The comparison of effective temperatures obtained from photometry and spectroscopy for the SDSS sample is presented in Figure 20. Overall, the photometric and spectroscopic temperatures agree surprisingly well, even at high temperatures where the energy distribution becomes insensitive to variations in  $T_{\text{eff}}$  in the optical (see also Figure 1). This lack of sensitivity of the *ugriz* photometry to effective temperature is most likely responsible for the increased dispersion observed above  $T_{\text{eff}} \sim 30,000$  K. The dispersion also becomes important near  $T_{\text{eff}} \sim 14,000$  K in the region where the strength of the hydrogen lines reach their maximum. As discussed in Section 3.4, our models predict stronger lines than those observed in the SDSS spectra, resulting in the large dispersion observed in Figure 20 in this particular temperature range.

Despite the overall agreement between spectroscopic and photometric temperatures, we can observe a small but significant temperature offset above  $T_{\text{eff}} \sim 14,000$  K, where spectroscopic temperatures appear systematically higher than those determined from photometry (about  $\sim 630$  K on average between 15,000 K and 40,000 K). Since the magnitudes have been corrected for interstellar reddening, and that this effect is particularly important at higher temperatures (see Figure 12), we need to test whether our correction procedure is responsible for the observed temperature offset. The importance of interstellar reddening is illustrated in Figure 21 where we show the same comparison between photometric and spectroscopic temperatures, but by using underreddened magnitudes. The temperature discrepancy becomes even more significant, especially at high effective temperatures, as expected. If anything, we can conclude that our procedure for taking into account the presence of interstellar reddening works fairly well.

We already discussed that the SDSS spectroscopic data suffer from a small calibration problem, and it is thus conceivable that this problem might be the origin of the temperature offset observed in Figure 20. Indeed, we already showed in Figure 19 that the effective temperatures above 14,000 K based on SDSS spectra appear *overestimated* with respect to those obtained from the Gianninas spectra. We can test this hypothesis by performing a similar experiment using the Gianninas spectroscopic sample. The first step is to search the SDSS database for white dwarfs in the Gianninas sample with measured *ugriz* photometry. Here we restrain our search to objects cooler than  $T_{\text{eff}} \sim 40,000$  K where the photometric technique is most sensitive. Since the SDSS is not an all-sky survey, not all stars in the Gianninas sample have measured *ugriz* photometry. To determine if an object is in the SDSS field, we first use the Simbad database<sup>9</sup> to obtain the positions of the stars in our sample,

---

<sup>9</sup><http://simbad.u-strasbg.fr/simbad/>

which are then fed into the SDSS Coverage Check tool<sup>10</sup>. We then compare the finding charts from the Villanova White Dwarf Catalog<sup>11</sup> with those from the SDSS website<sup>12</sup> to obtain the position of the stars in the SDSS database, and enter these positions in the Imaging Query<sup>13</sup> to retrieve the required *ugriz* photometric data. The use of finding charts was preferred to simply entering the Simbad positions directly in the Imaging Query, a procedure that resulted in a lot of mismatches. Following these steps, we identified 561 white dwarfs in the Gianninas sample with measured *ugriz* photometry; we will refer to this particular sample as the *Gianninas subset*. By the same token, we obtain the corresponding SDSS spectrum, if available, from the same tool. As previously mentioned in Section 3.4, 200 of the 561 white dwarfs in the Gianninas subset also had a measured SDSS spectrum.

The comparison of effective temperatures obtained from photometry and spectroscopy for the Gianninas subset is presented in the left panel of Figure 22. For an easier comparison, we reproduce in the right panel the results obtained from the SDSS sample on the same scale. Unfortunately, the temperature offset is still present using the Gianninas subset, and extends to even lower effective temperatures ( $T_{\text{eff}} \sim 10,000$  K) than with the SDSS sample. The average difference between spectroscopic and photometric temperatures for  $15,000 \text{ K} < T_{\text{eff}} < 40,000 \text{ K}$  is about 580 K for the Gianninas subset, only  $\sim 50$  K smaller than the difference observed with the SDSS sample. Note that the effect of interstellar reddening is almost completely negligible for the Gianninas subset (not shown here), with the exception of the hottest stars, since most white dwarfs in this sample are relatively bright and nearby. Given that we demonstrated that the *ugriz* photometry has been properly calibrated and dereddened, and given that we took into account the appropriate 3D hydrodynamical corrections in our spectroscopic analysis, we are left with little explanation to account for the observed temperature offset. Note that a similar offset was also reported in the comparison performed by Tremblay et al. (2013, see their Figure 16).

Since the spectroscopic technique is more sensitive than the photometric technique to the details of model atmosphere calculations, in particular the line broadening theory, the occupation probability formalism, etc., we perform a final test using a different set of model spectra. Here we rely on the model atmospheres and synthetic spectra described at length in Liebert et al. (2005) and references therein. These are based on the Stark profiles from Lemke (1997), while our current model spectra rely on the improved Stark profile calcu-

---

<sup>10</sup><http://dr10.mirror.sdss3.org/coverageCheck/search>

<sup>11</sup><http://www.astronomy.villanova.edu/WDcatalog/>

<sup>12</sup><http://skyserver.sdss3.org/dr10/en/tools/chart/navi.aspx>

<sup>13</sup><http://skyserver.sdss3.org/dr10/en/tools/search/IQS.aspx>

lations from Tremblay & Bergeron (2009), which take into account nonideal perturbations from protons and electrons — described within the occupation probability formalism of Hummer & Mihalas (1988) — directly inside the line profile calculations. To compensate for the neglect of these nonideal effects in the previous Stark broadening tables, Bergeron (1993) suggested to include an ad hoc parameter to *mimic* the nonideal effects in the line profiles, more specifically, by taking twice the value of the critical electric microfield ( $\beta_{\text{crit}}$ ) in the Hummer-Mihalas theory (see Tremblay & Bergeron 2009 for a full discussion of this approach). By doing so, it was found that the internal consistency between the spectroscopic solutions obtained when increasing the number of Balmer lines in the fitting procedure was improved substantially. As also mentioned by Tremblay & Bergeron, however, we must emphasize that this is just a quick and dirty way to simulate the nonideal effects by reducing the line wing opacity, and this does not imply that Hummer & Mihalas underestimated the value of the critical field in any way. The approach described in Tremblay & Bergeron (2009) where the Hummer-Mihalas formalism is included directly into the line profile calculation, without any modification to  $\beta_{\text{crit}}$ , is more physically sound by any standard.

This being said, we redetermined self-consistently the photometric and spectroscopic effective temperatures using this older generation of model spectra. The results for the Gianninas subset, which appears to be better calibrated than the SDSS sample, are shown in Figure 23. First of all, the temperature offset apparent in Figure 22 has been significantly reduced above  $T_{\text{eff}} \sim 20,000$  K, if not eliminated, but another offset has now developed between  $T_{\text{eff}} = 13,000$  K and  $19,000$  K, where the photometric temperatures now exceed the spectroscopic values. The average difference between spectroscopic and photometric temperatures for  $15,000 \text{ K} < T_{\text{eff}} < 40,000 \text{ K}$  is now  $-190$  K. Even though we do not claim that the model spectra described in Liebert et al. (2005) are more appropriate than those used here, the results of our experiment nevertheless suggest that the physics of line broadening may still require some improvement.

## 5. Surface Gravity Determinations using Photometric Data

As shown in Figure 1, the strength of the Balmer jump, as measured by the  $u - g$  color index, is very sensitive to surface gravity in a certain range of effective temperature ( $8000 \text{ K} \lesssim T_{\text{eff}} \lesssim 17,000 \text{ K}$ ). Weidemann (1971, see also Shipman & Sass 1980) successfully explained this behavior in terms of a competition between bound-free atomic hydrogen and free-free  $\text{H}^-$  opacities. We attempt in this section to exploit this particular sensitivity to  $\log g$  to measure surface gravities using the photometric technique, an approach similar to that described by Koester et al. (2009a).

In order to determine the surface gravities for the white dwarfs in the SDSS sample using photometry, we simply modify the photometric technique described in Section 2.2 by adding a third fitting parameter,  $\log g$ , to the two existing ones — the effective temperature  $T_{\text{eff}}$  and the solid angle  $\pi(R/D)^2$ . Note that unless the distance  $D$  is known from a trigonometric parallax measurement,  $\log g$  and  $\pi(R/D)^2$  are independent parameters. To achieve a better convergence of the  $\chi^2$  minimization procedure, we obtain a first estimate of the effective temperature by assuming  $\log g = 8.0$ , and then we let all three parameters vary. Interstellar reddening is also taken into account following the same procedure as before.

The atmospheric parameters obtained from this modified photometric technique are displayed in Figure 24; note that we do not show here objects for which  $\chi_{\text{red}}^2 > \chi_{\text{crit}}^2$ . Also, we restrict our analysis to white dwarfs with  $8000 \text{ K} < T_{\text{eff}} < 17,000 \text{ K}$  where the sensitivity of the Balmer jump to surface gravity is most important. Our results reveal that the photometric  $\log g$  distribution follows the  $0.598 M_{\odot}$  evolutionary track quite well, but the scatter is admittedly significant. The dispersion in  $\log g$  has a distinctive butterfly shape, which reaches a minimum around  $T_{\text{eff}} = 12,000 \text{ K}$  where the sensitivity of the  $u - g$  color index to  $\log g$  becomes maximal. More interestingly, the high- $\log g$  problem observed in the top panel of Figures 14 and 15 is not present in the photometric  $\log g$  distribution, which indicates that the 3D hydrodynamical effects do not affect the region where the continuum is formed, but have an effect mostly on the shape of the absorption lines, as discussed by Tremblay et al. (2013). Consequently, photometric results remain unaffected by the particular treatment of convective energy transport at low effective temperatures.

For comparison, we also reproduce in Figure 24 the spectroscopic temperatures and surface gravities (corrected for 3D effects) for the same objects. It is not surprising to see here that the dispersion of the spectroscopic distribution is much smaller than that obtained from photometry, since the spectroscopic technique is arguably more precise (but not necessarily more accurate) than any other method for measuring atmospheric parameters (see, e.g., Bergeron et al. 1992). We explore this more quantitatively in Figure 25 where the photometric and spectroscopic  $\log g$  distributions are plotted as histograms. As expected from the results shown in Figure 24, both distributions peak around  $\log g = 8.0$ , with  $\langle \log g_{\text{phot}} \rangle = 7.994$  and  $\langle \log g_{\text{spec}} \rangle = 8.037$ , but the dispersion using the photometric technique ( $\sigma_{\text{phot}} = 0.404$ ) is much more important than that obtained from spectroscopy ( $\sigma_{\text{spec}} = 0.206$ ). Nevertheless, our results indicate that it is still possible to get a reasonable estimate of the surface gravity using only photometry.

As mentioned above, Koester et al. (2009a) used a similar approach to measure the atmospheric parameters of bright ( $g < 19$ ) DA white dwarfs from the fourth data release (DR4) of the SDSS (see their Figure 2). Unlike our photometric  $\log g$  distribution shown

in Figure 24, which follows the evolutionary track extremely well, their photometric  $\log g$  distribution still shows a small high- $\log g$  problem between  $T_{\text{eff}} \sim 12,000$  K and 9000 K, although less important than that observed in the corresponding spectroscopic  $\log g$  distribution. Moreover, their surface gravities are systematically lower than the mean value of  $\log g = 8.0$ , regardless of effective temperature, unlike our distribution shown in Figure 24.

## 6. Summary and Conclusions

We tested the calibration of the *ugriz* photometric system by using hydrogen-line DA white dwarfs from the Data Release 7 of the Sloan Digital Sky Survey. We first had to ensure that our sample was clean and contained only objects with good measured *ugriz* photometry. To achieve this, we first limited the DA sample to objects with a signal-to-noise ratio above 25 in the *g*-band and  $\sigma_{m_\nu} < 0.1$  in all bandpasses. Since our photometric technique is based on a  $\chi^2$  minimization method, we then defined a value  $\chi_{\text{crit}}^2$  above which the atmospheric parameters were considered inaccurate. By examining the photometric fits and their corresponding reduced  $\chi^2$  values, we arbitrarily determined that a critical value of  $\chi_{\text{crit}}^2 = 3$  allowed us to exclude most of the bad data from our photometric sample. In order to test the photometric calibration, we first verified that the photometric temperatures were not affected by the red leak in the *u* filter, or by the assumption of  $\log g = 8.0$  in our photometric fits. We then compared the observed and predicted magnitudes in each of the five bandpasses, and we concluded that, when the proper SDSS to AB<sub>95</sub> corrections are applied, the *ugriz* photometric system appears well calibrated.

We then defined two spectroscopic samples: the SDSS sample, which contains the same white dwarfs as the photometric sample, and the Gianninas sample, based on the bright ( $V \leq 17.5$ ) DA white dwarfs from the Villanova White Dwarf Catalog. Using these two samples, we first explored the well known high- $\log g$  problem at low effective temperatures, which can be effectively corrected by applying the 3D correction functions recently published by Tremblay et al. (2013). We then compared the atmospheric parameters obtained for the objects in common between the SDSS and Gianninas data sets, and concluded that the SDSS spectra may still have a small calibration problem, despite the improvements in their data reduction algorithm.

The next step in our analysis was to compare the atmospheric parameters obtained from photometry and spectroscopy. Using the SDSS photometric and spectroscopic samples, we observed that a systematic offset appeared above  $T_{\text{eff}} \sim 14,000$  K, where photometric temperatures are systematically lower than the spectroscopic values. This temperature offset cannot be fully explained by the calibration problem of the SDSS spectra since it is also

present when using the Gianninas spectra. This offset does not appear to be related to our procedure for taking into account the presence of interstellar reddening either, since the Gianninas sample, where the offset is also observed, contains bright, and mostly nearby white dwarfs, which are not affected by reddening. Hence, the origin of this small discrepancy still eludes us, but could be related to the physics of the model spectra used in the spectroscopic method.

Finally, we exploited the sensitivity of the Balmer jump to surface gravity between  $T_{\text{eff}} \sim 8000$  K and 17,000 K to measure  $\log g$  values using the photometric method. Our results showed that, even if photometric  $\log g$  values are less precise than spectroscopic values, it is still possible to obtain a good estimate of the  $\log g$  distribution using the photometric technique. In particular, we showed that the high- $\log g$  problem is not observed in the  $\log g$  distribution derived from photometry, confirming that this problem is related to the hydrogen line profiles predicted from 1D/MLT model atmospheres.

We would like to thank A. Darveau-Bernier for his earlier contribution to this project. This work was supported in part by the NSERC Canada and by the Fund FRQ-NT (Québec). This research has made use of the SIMBAD database, operated at CDS, Strasbourg, France.

## REFERENCES

- Abazajian, K. N., Adelman-McCarthy, J. K., Agüeros, M. A., Allam, S. S., Allende Prieto, C., An, D., Anderson, K. S. J., Anderson, S. F., Annis, J., Bahcall, N. A., & et al. 2009, *ApJS*, 182, 543
- Bergeron, P. 1993, in *NATO ASIC Proc. 403: White Dwarfs: Advances in Observation and Theory*, ed. M. A. Barstow, 267
- Bergeron, P., Leggett, S. K., & Ruiz, M. T. 2001, *ApJS*, 133, 413
- Bergeron, P., Ruiz, M. T., & Leggett, S. K. 1997, *ApJS*, 108, 339
- Bergeron, P., Saffer, R. A., & Liebert, J. 1992, *ApJ*, 394, 228
- Bergeron, P., Saumon, D., & Wesemael, F. 1995a, *ApJ*, 443, 764
- Bergeron, P., Wesemael, F., Dufour, P., Beauchamp, A., Hunter, C., Saffer, R. A., Gianninas, A., Ruiz, M. T., Limoges, M.-M., Dufour, P., Fontaine, G., & Liebert, J. 2011, *ApJ*, 737, 28

- Bergeron, P., Wesemael, F., & Fontaine, G. 1991, *ApJ*, 367, 253
- Bergeron, P., Wesemael, F., Lamontagne, R., Fontaine, G., Saffer, R. A., & Allard, N. F. 1995b, *ApJ*, 449, 258
- Dantona, F. & Mazzitelli, I. 1979, *A&A*, 74, 161
- Doi, M., Tanaka, M., Fukugita, M., Gunn, J. E., Yasuda, N., Ivezić, Ž., Brinkmann, J., de Haars, E., Kleinman, S. J., Krzesinski, J., & French Leger, R. 2010, *AJ*, 139, 1628
- Eisenstein, D. J., Liebert, J., Harris, H. C., Kleinman, S. J., Nitta, A., Silvestri, N., Anderson, S. A., Barentine, J. C., Brewington, H. J., Brinkmann, J., Harvanek, M., Krzesiński, J., Neilsen, Jr., E. H., Long, D., Schneider, D. P., & Snedden, S. A. 2006, *ApJS*, 167, 40
- Fan, X., Strauss, M. A., Richards, G. T., Newman, J. A., Becker, R. H., Schneider, D. P., Gunn, J. E., Davis, M., White, R. L., Lupton, R. H., Anderson, Jr., J. E., Annis, J., Bahcall, N. A., Brunner, R. J., Csabai, I., Doi, M., Fukugita, M., Hennessy, G. S., Hindsley, R. B., Ivezić, Ž., Knapp, G. R., McKay, T. A., Munn, J. A., Pier, J. R., Szalay, A. S., & York, D. G. 2001, *AJ*, 121, 31
- Fontaine, G., Brassard, P., & Bergeron, P. 2001, *PASP*, 113, 409
- Gianninas, A., Bergeron, P., & Ruiz, M. T. 2011, *ApJ*, 743, 138
- Harris, H. C., Munn, J. A., Kilic, M., Liebert, J., Williams, K. A., von Hippel, T., Levine, S. E., Monet, D. G., Eisenstein, D. J., Kleinman, S. J., Metcalfe, T. S., Nitta, A., Winget, D. E., Brinkmann, J., Fukugita, M., Knapp, G. R., Lupton, R. H., Smith, J. A., & Schneider, D. P. 2006, *AJ*, 131, 571
- Holberg, J. B. & Bergeron, P. 2006, *AJ*, 132, 1221
- Hubeny, I. & Lanz, T. 1995, *ApJ*, 439, 875
- Hummer, D. G. & Mihalas, D. 1988, *ApJ*, 331, 794
- Kilic, M., Leggett, S. K., Tremblay, P.-E., von Hippel, T., Bergeron, P., Harris, H. C., Munn, J. A., Williams, K. A., Gates, E., & Farihi, J. 2010, *ApJS*, 190, 77
- Kleinman, S. J., Kepler, S. O., Koester, D., Pelisoli, I., Peçanha, V., Nitta, A., Costa, J. E. S., Krzesinski, J., Dufour, P., Lachapelle, F.-R., Bergeron, P., Yip, C.-W., Harris, H. C., Eisenstein, D. J., Althaus, L., & Córscico, A. 2013, *ApJS*, 204, 5
- Koester, D. 1976, *A&A*, 52, 415

- Koester, D., Kepler, S. O., Kleinman, S. J., & Nitta, A. 2009a, *Journal of Physics Conference Series*, 172, 012006
- Koester, D., Voss, B., Napiwotzki, R., Christlieb, N., Homeier, D., Lisker, T., Reimers, D., & Heber, U. 2009b, *A&A*, 505, 441
- Lemke, M. 1997, *A&AS*, 122, 285
- Liebert, J., Bergeron, P., & Holberg, J. B. 2005, *ApJS*, 156, 47
- McCook, G. P. & Sion, E. M. 1999, *ApJS*, 121, 1
- Press, W. H., Flannery, B. P., & Teukolsky, S. A. 1986, *Numerical recipes. The art of scientific computing*, ed. Press, W. H., Flannery, B. P., & Teukolsky, S. A.
- Shipman, H. L. & Sass, C. A. 1980, *ApJ*, 235, 177
- Tremblay, P.-E. & Bergeron, P. 2009, *ApJ*, 696, 1755
- Tremblay, P.-E., Bergeron, P., & Gianninas, A. 2011a, *ApJ*, 730, 128
- Tremblay, P.-E., Bergeron, P., Kalirai, J. S., & Gianninas, A. 2010, *ApJ*, 712, 1345
- Tremblay, P.-E., Ludwig, H.-G., Steffen, M., Bergeron, P., & Freytag, B. 2011b, *A&A*, 531, L19
- Tremblay, P.-E., Ludwig, H.-G., Steffen, M., & Freytag, B. 2013, *A&A*, 559, A104
- Vauclair, G. & Reisse, C. 1977, *A&A*, 61, 415
- Vennes, S., Thejll, P. A., Génova Galvan, R., & Dupuis, J. 1997, *ApJ*, 480, 714
- Voss, B., Koester, D., Napiwotzki, R., Christlieb, N., & Reimers, D. 2007, *A&A*, 470, 1079
- Weidemann, V. 1971, in *IAU Symposium, Vol. 42, White Dwarfs*, ed. W. J. Luyten, 81



Fig. 1.—  $(u - g, g - r)$  two-color diagram for hydrogen-atmosphere white dwarfs with  $T_{\text{eff}}$  indicated in units of  $10^3$  K, and  $\log g$  values of 7.0 (0.5) 9.5 (from bottom to top). The observed *ugriz* photometry is taken from Kleinman et al. (2013).

Fig. 2.— Examples of fits using the photometric technique. Error bars show the observed *ugriz* photometry while the dots represent the best model fit. The effective temperature, surface gravity, and reduced  $\chi^2$  values are also given in each panel. Since no parallax measurements are available for these stars, we assume  $\log g = 8.0$  throughout.

Fig. 3.— Reduced  $\chi^2$  distribution obtained with the photometric technique using *ugriz* photometry for the SDSS sample and by assuming  $\log g = 8.0$ . Objects with  $\chi_{\text{red}}^2 > 15$  are not displayed here.

Fig. 4.— Transmission curves for the SDSS *ugriz* filters as measured by Jim Gunn in 2001 (dashed curves) and Doi et al. (2010, solid curves); all transmission curves are normalized to unity. Both sets include the extinction through an air mass of 1.3. Note that the transmission curves from Gunn do not include the complete system response from atmosphere to detector.

Fig. 5.— Comparison of effective temperatures obtained using the transmission curves from Gunn in 2001 and from Doi et al. (2010) for the SDSS sample. Objects for which  $\chi_{\text{red}}^2 > \chi_{\text{crit}}^2$  are shown in red. The dashed line represents the 1:1 correspondence.

Fig. 6.— Comparison of effective temperatures obtained with the photometric technique using *ugriz* and *griz* photometry for the SDSS sample. Surface gravities are assumed to be  $\log g = 8.0$ . Objects for which  $\chi_{\text{red}}^2 > \chi_{\text{crit}}^2$  are shown in red. The thick solid line represents the 1:1 correspondence.

Fig. 7.— Comparison of effective temperatures obtained with the photometric technique by assuming  $\log g = 8.0$  and by adopting the surface gravity determined spectroscopically, for the SDSS sample. Objects for which  $\chi_{\text{red}}^2 > \chi_{\text{crit}}^2$  are shown in red. The dashed line represents the 1:1 correspondence.

Fig. 8.— Histograms showing the difference between the observed (obs) magnitudes and those predicted by the photometric technique (th). SDSS to AB<sub>95</sub> corrections from Eisenstein et al. (2006) have been applied. Only objects with  $T_{\text{eff}} < 20,000$  K are considered here. The thick dashed lines correspond to  $m_{\nu, \text{obs}} = m_{\nu, \text{th}}$ .

Fig. 9.— Same as Figure 8 but without the SDSS to AB<sub>95</sub> corrections applied.

Fig. 10.— Differences between the observed (obs) magnitudes and those predicted by the photometric technique (th) as a function of the observed magnitude. SDSS to AB<sub>95</sub> correc-

tions from Eisenstein et al. (2006) have been applied. The red circles represent objects with  $T_{\text{eff}} > 20,000$  K. The dashed lines correspond to  $m_{\nu,\text{obs}} = m_{\nu,\text{th}}$ .

Fig. 11.— Distribution of white dwarf distances in the SDSS derived from the photometric technique but by adopting the spectroscopic  $\log g$  values rather than assuming  $\log g = 8$ . Objects for which  $\chi_{\text{red}}^2 > \chi_{\text{crit}}^2$  are not considered here.

Fig. 12.— Comparison between effective temperatures obtained with underreddened and dereddened magnitudes, for the SDSS sample. The thick solid line represents the 1:1 correspondence. Objects for which  $\chi_{\text{red}}^2 > \chi_{\text{crit}}^2$  are shown in red.

Fig. 13.— Examples of fits obtained with the spectroscopic technique. The black lines show the observed spectrum, while the red lines correspond to the model fit. Lines range from  $H\beta$  (bottom) to  $H8$  (top) and are offset vertically for clarity. The effective temperature and surface gravity (uncorrected for 3D effects) of each star are also given. Examples of problematic SDSS spectra are shown at the bottom.

Fig. 14.— Top panel: Atmospheric parameters for the SDSS spectroscopic sample determined with the spectroscopic technique using 1D/MLT models, for  $30,000 \text{ K} \geq T_{\text{eff}} \geq 6000 \text{ K}$ . Bottom panel: Same results but with the 3D hydrodynamical corrections from Tremblay et al. (2013). The dashed line in both panels shows a  $0.592 M_{\odot}$  evolutionary track, which corresponds to the median mass (corrected) for this sample in this temperature range.

Fig. 15.— Same as Figure 14 but for the Gianninas sample. The dashed line shows a  $0.616 M_{\odot}$  evolutionary track, which corresponds to the median mass (corrected) for this sample in this temperature range.

Fig. 16.— Differences in surface gravity (top panel) and effective temperature (bottom panel) between 1D/MLT models ( $ML2/\alpha = 0.7$ ) and 3D hydrodynamical models from Tremblay et al. (2013), for  $7.0 < \log g < 9.0$  and  $20,000 \text{ K} > T_{\text{eff}} > 5000 \text{ K}$ .

Fig. 17.— Mass distributions for the SDSS spectroscopic sample obtained without (left) and with (right) the 3D correction functions from Tremblay et al. (2013). The black histograms show the total sample, while the blue ones correspond to objects with  $T_{\text{eff}} > 13,000 \text{ K}$  and the red ones to objects with  $T_{\text{eff}} < 13,000 \text{ K}$ . The mean masses and standard deviations (in solar mass units) of the corresponding samples are also given.

Fig. 18.— Same as Figure 17 but for the Gianninas spectroscopic sample.

Fig. 19.— Comparison of effective temperatures obtained with the spectroscopic method

between the SDSS and Gianninas samples. Correction functions from Tremblay et al. (2013) have been applied. The dashed line represents the 1:1 correspondence.

Fig. 20.— Comparison between effective temperatures obtained from photometry and spectroscopy for the SDSS sample. Magnitudes have been corrected for interstellar reddening. Objects for which  $\chi_{\text{red}}^2 > \chi_{\text{crit}}^2$  are shown in red. The thick solid line represents the 1:1 correspondence.

Fig. 21.— Same as Figure 20 but magnitudes have not been corrected for interstellar reddening.

Fig. 22.— Left panel: Comparison between effective temperatures obtained from photometry and spectroscopy for the Gianninas subset (see text). Magnitudes have been corrected for interstellar reddening. Objects for which  $\chi_{\text{red}}^2 > \chi_{\text{crit}}^2$  are shown in red. The thick solid line represents the 1:1 correspondence. Right panel: Same as the left panel but for the SDSS sample.

Fig. 23.— Comparison of effective temperatures obtained from photometry and spectroscopy for the Gianninas subset using Stark profiles from Lemke (1997) and twice the value of the critical microfield  $\beta_{\text{crit}}$  (see text). Magnitudes have been corrected for interstellar reddening. Objects for which  $\chi_{\text{red}}^2 > \chi_{\text{crit}}^2$  are shown in red. The thick solid line represents the 1:1 correspondence.

Fig. 24.— Atmospheric parameters for the SDSS sample obtained from photometry (black circles) by exploiting the sensitivity of the Balmer jump ( $u - g$  color index) to  $\log g$  between 8000 K and 17,000 K. Magnitudes have been corrected for interstellar reddening. Objects for which  $\chi_{\text{red}}^2 > \chi_{\text{crit}}^2$  are not shown here. The dashed line shows a  $0.592 M_{\odot}$  evolutionary track, which is the median mass for the SDSS sample in this temperature range. The red dots show the spectroscopic results for the same objects.

Fig. 25.— Photometric (black) and spectroscopic (red)  $\log g$  distributions for white dwarfs in the SDSS with  $8000 \text{ K} < T_{\text{eff}} < 17,000 \text{ K}$ . The spectroscopic  $\log g$  values have been corrected for 3D hydrodynamical effects.

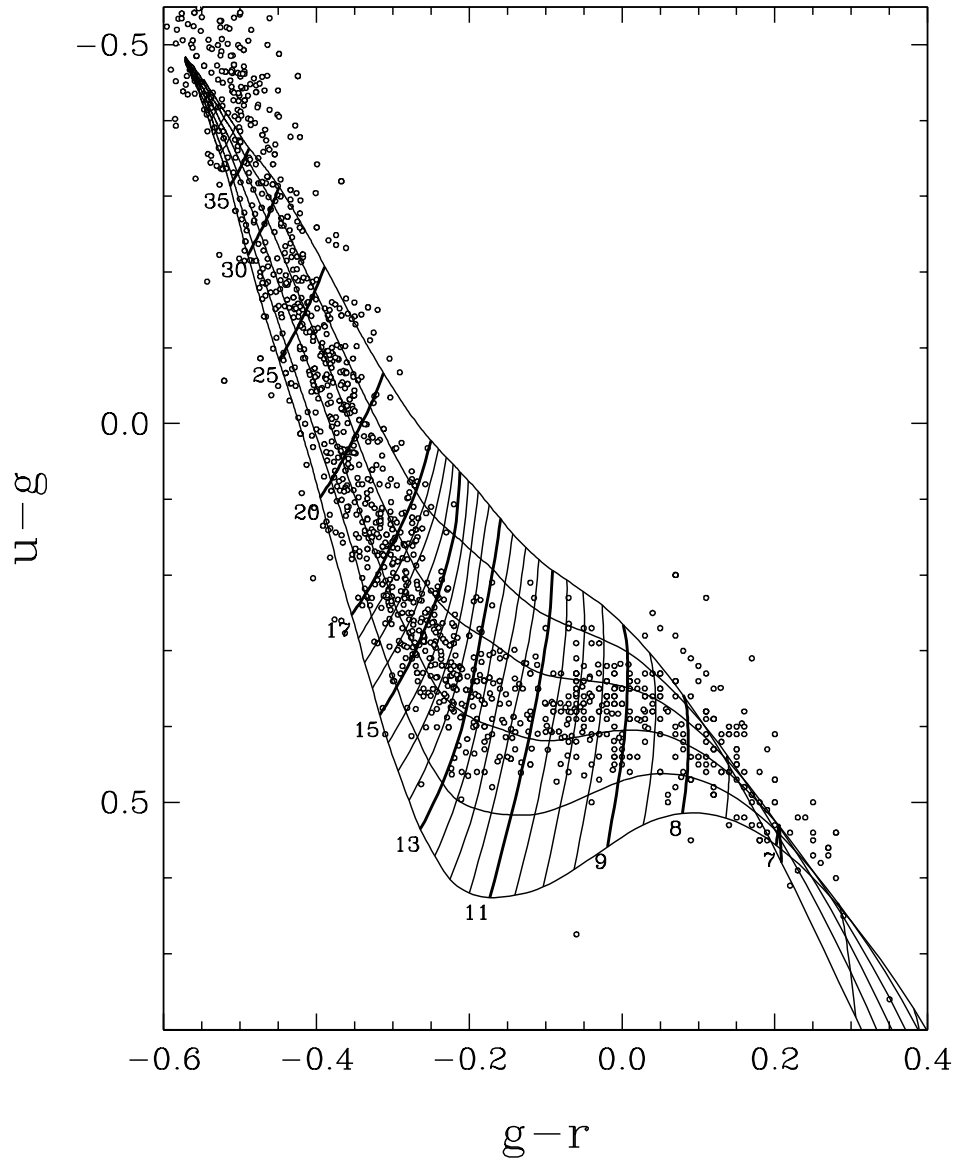


Figure 1

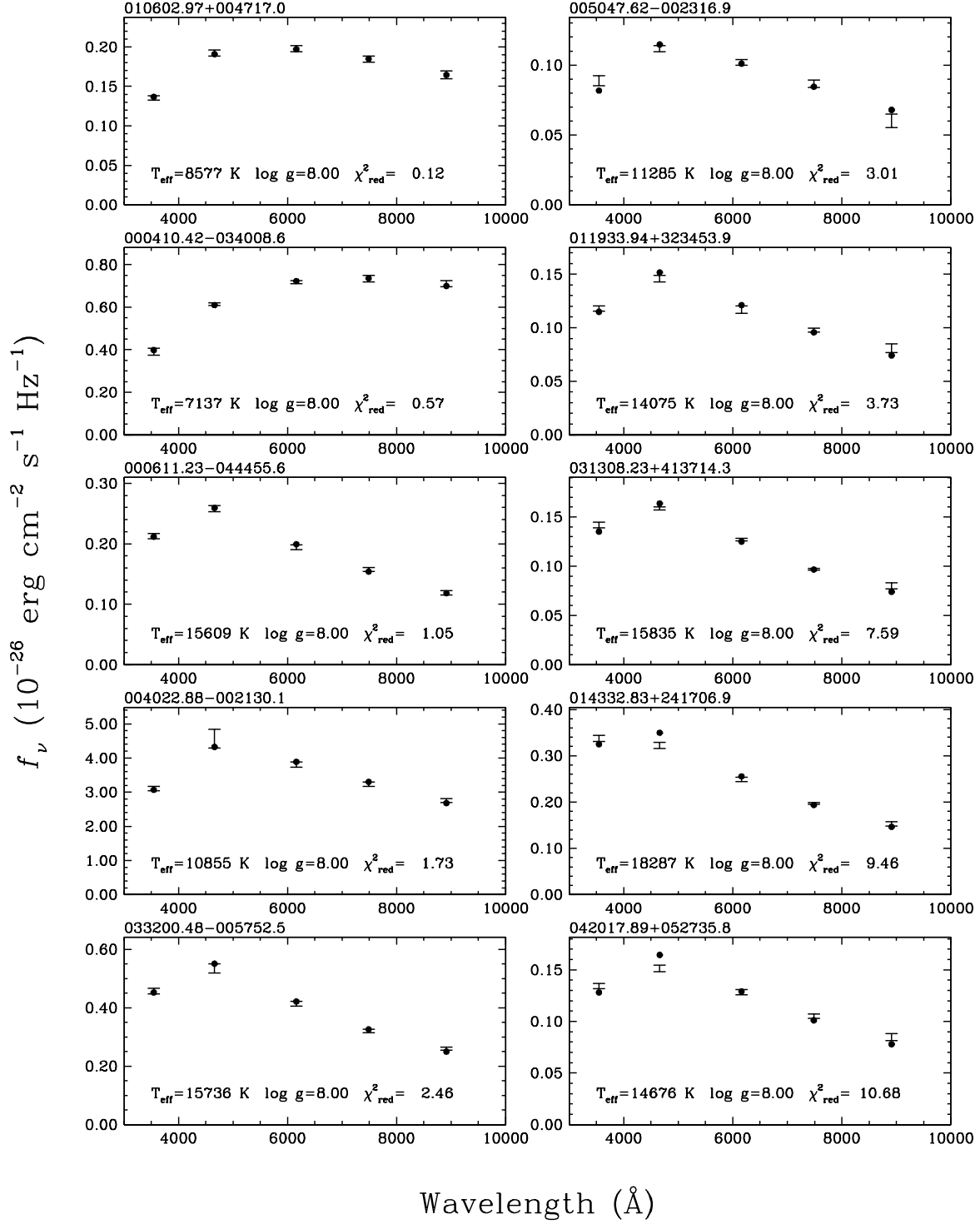


Figure 2

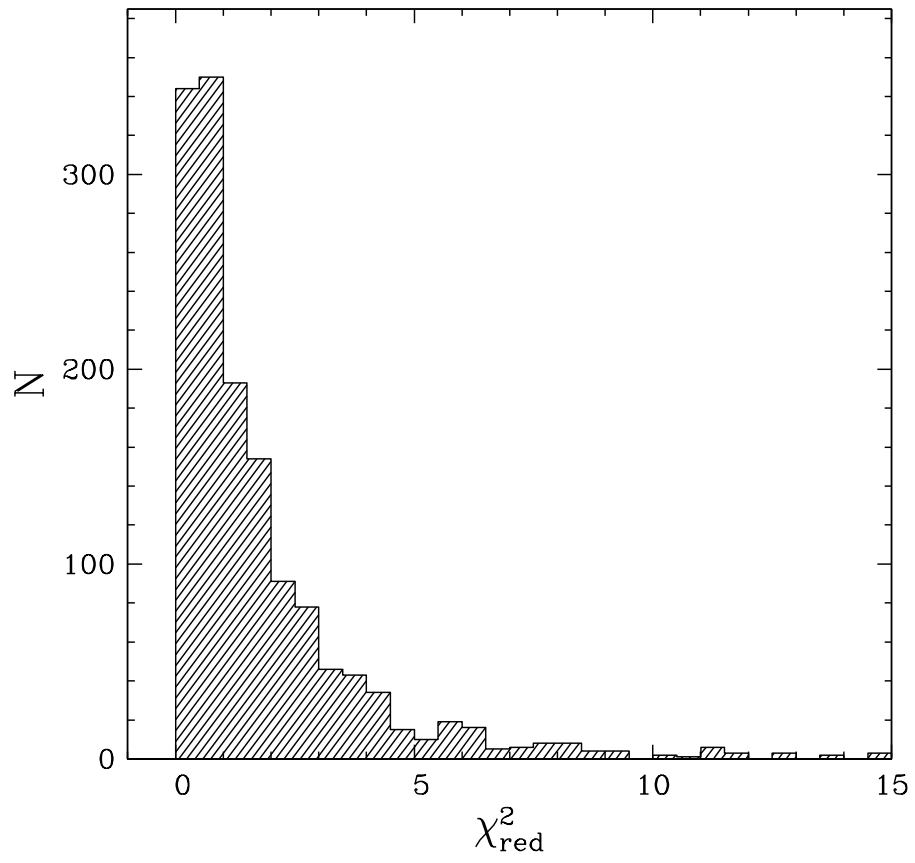


Figure 3

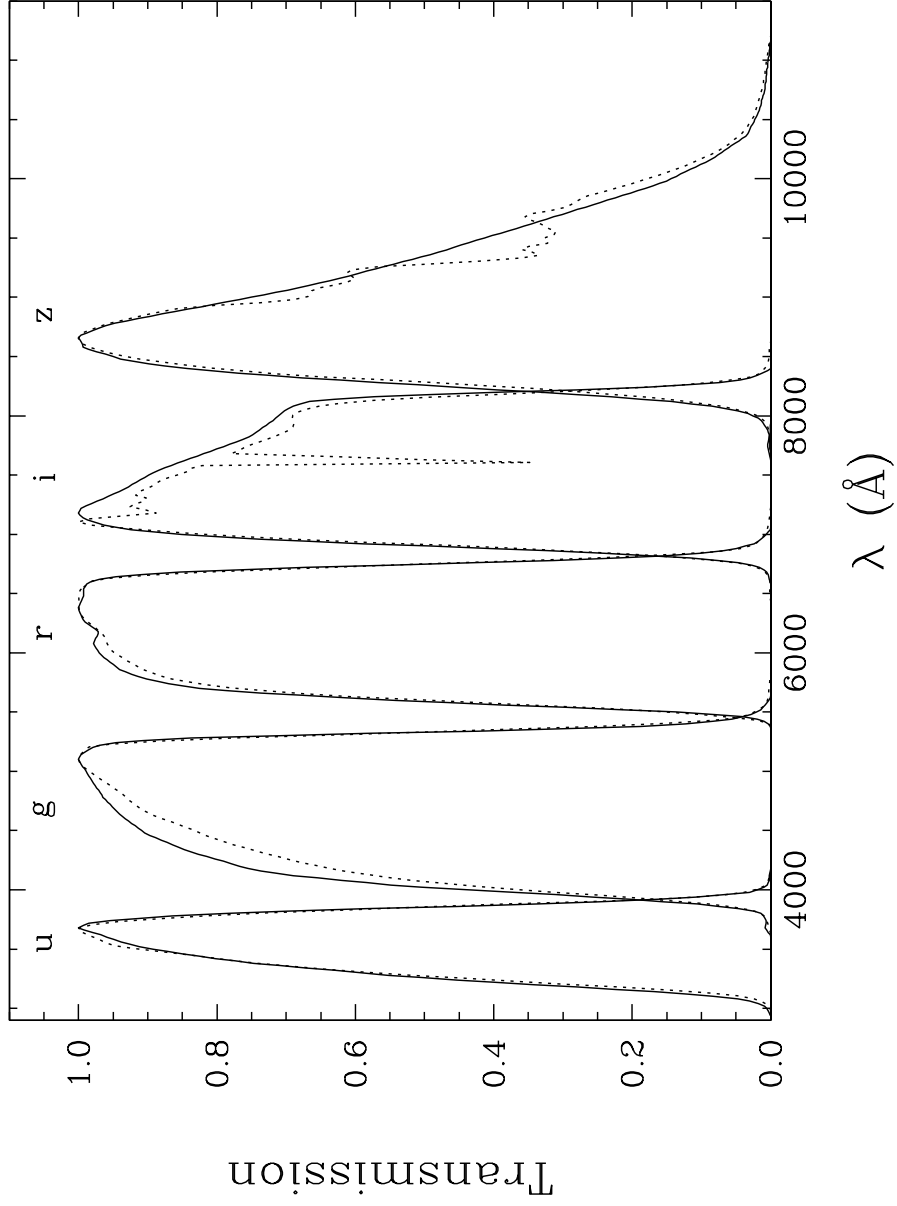


Figure 4

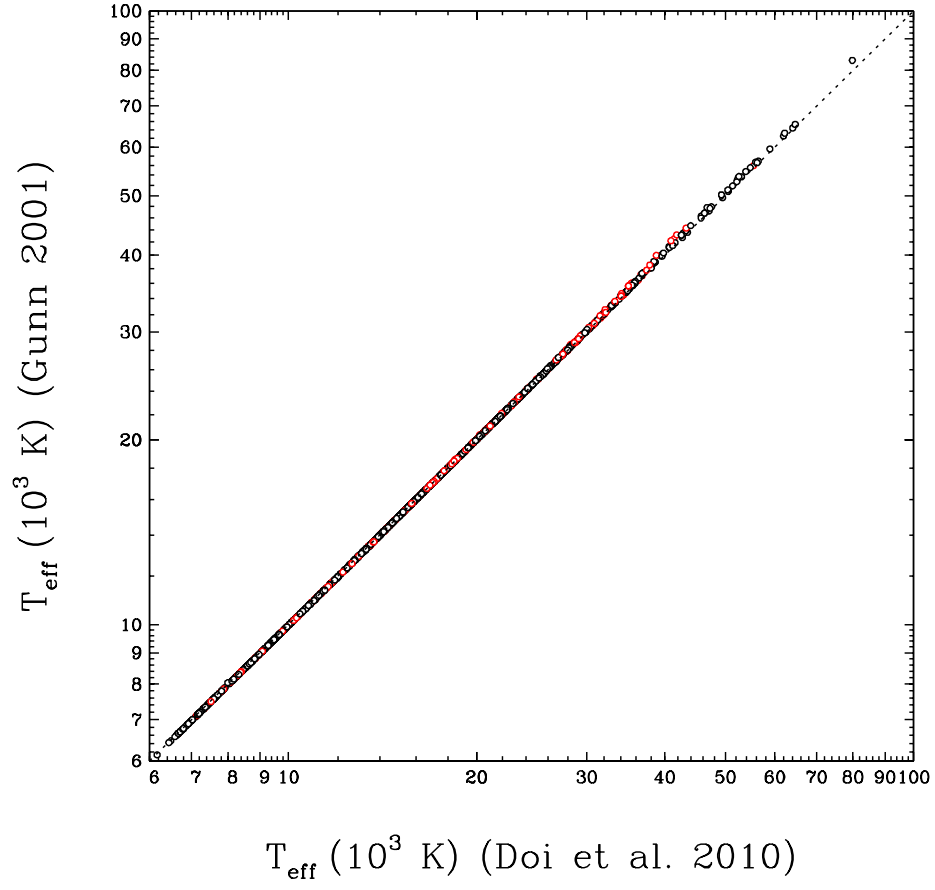


Figure 5



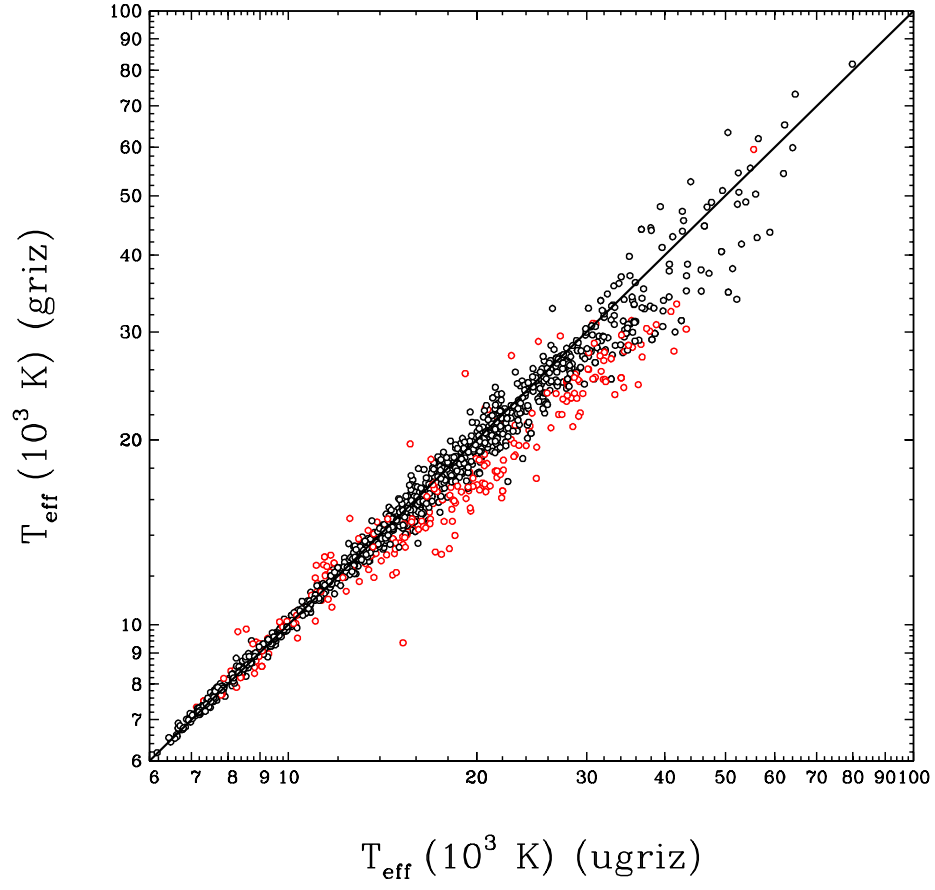


Figure 6

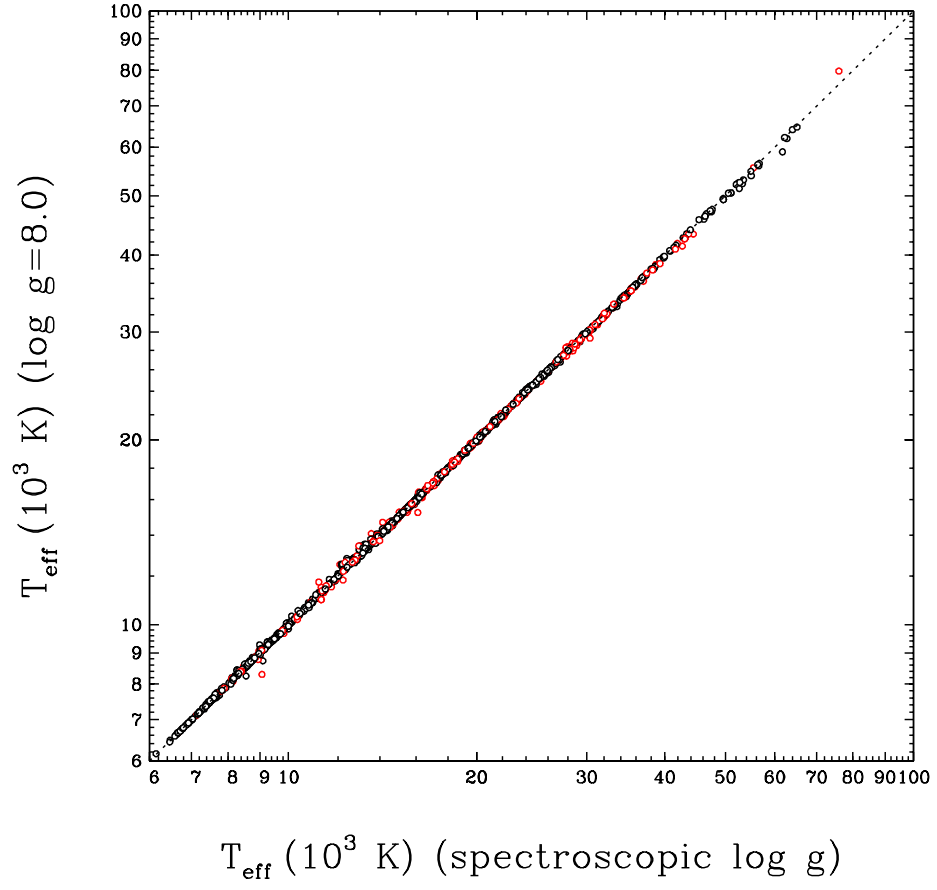


Figure 7

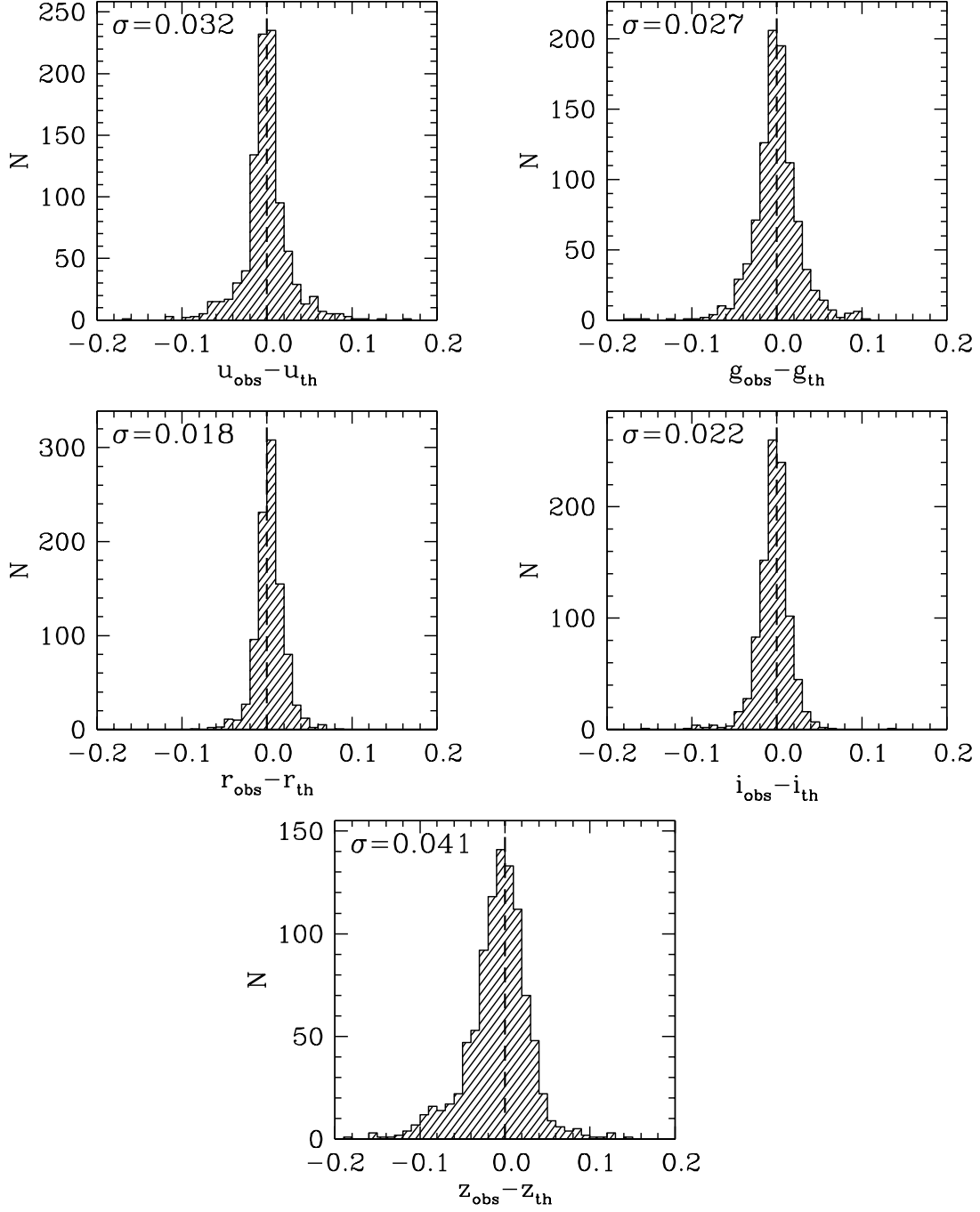


Figure 8

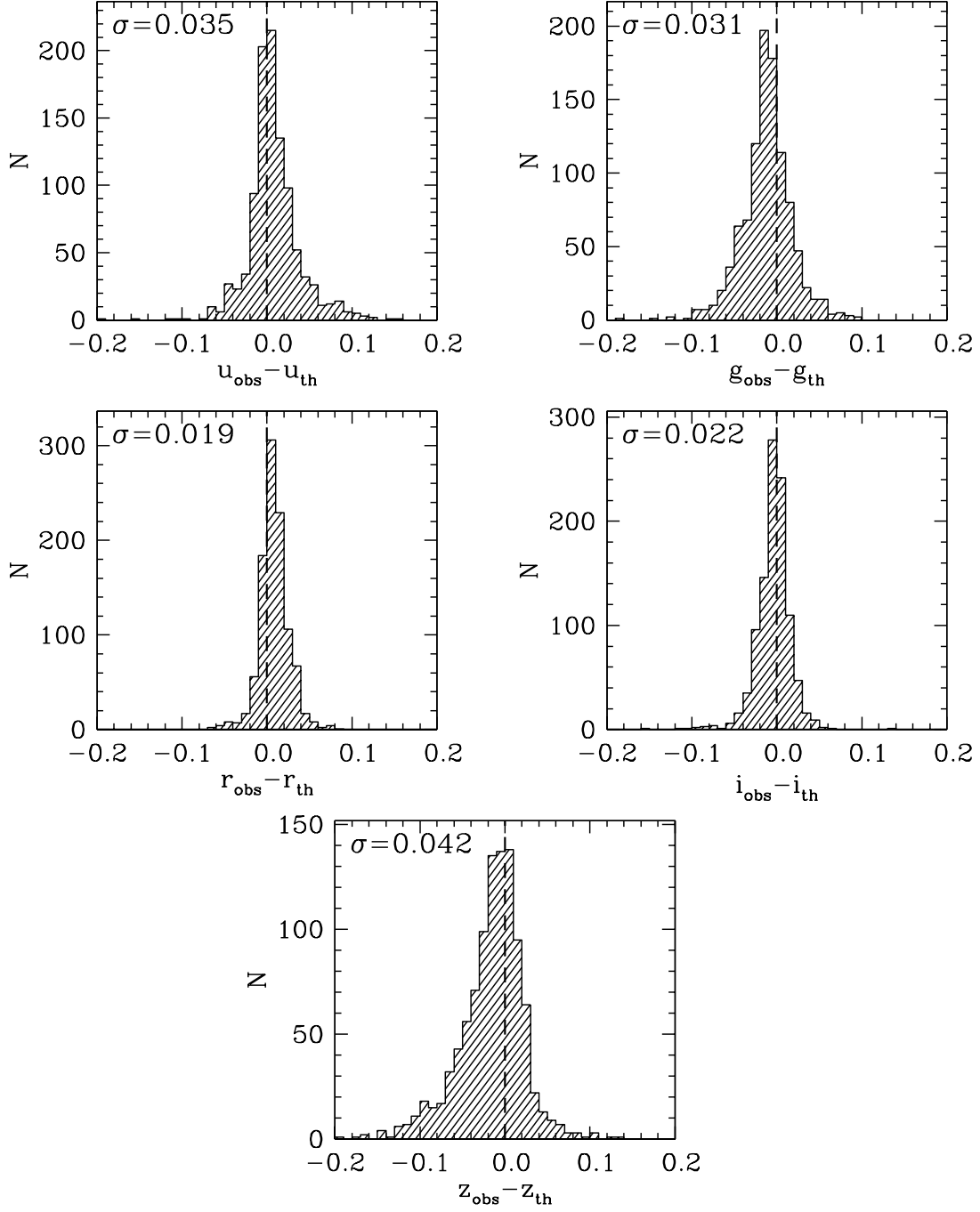


Figure 9

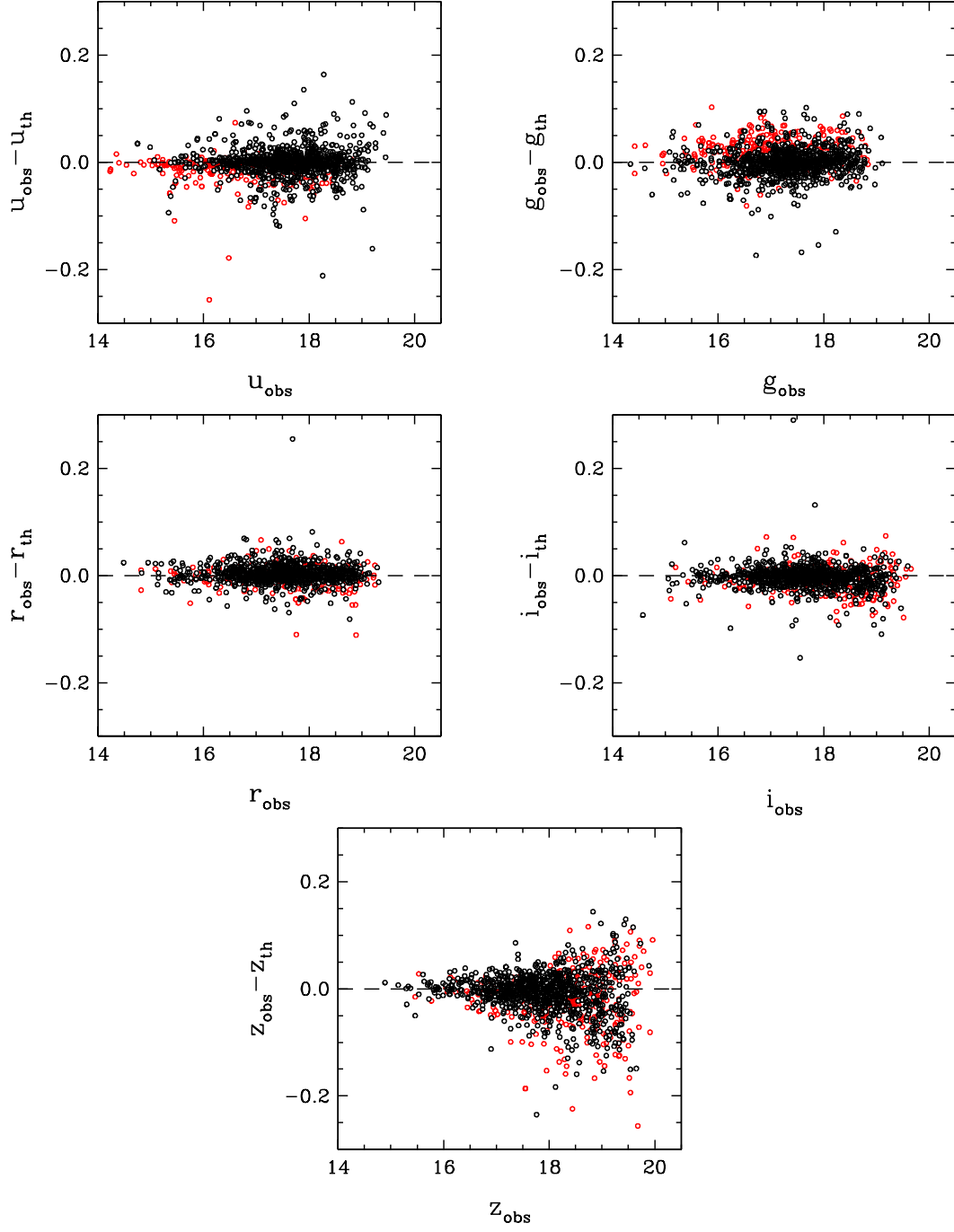


Figure 10

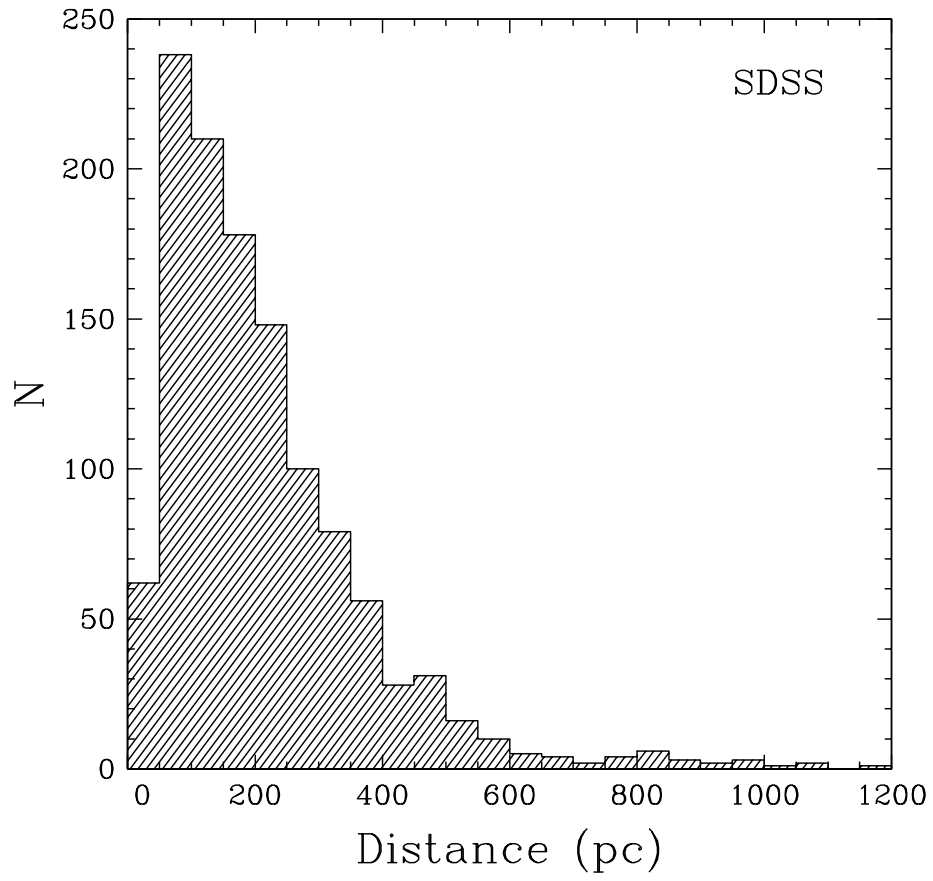


Figure 11

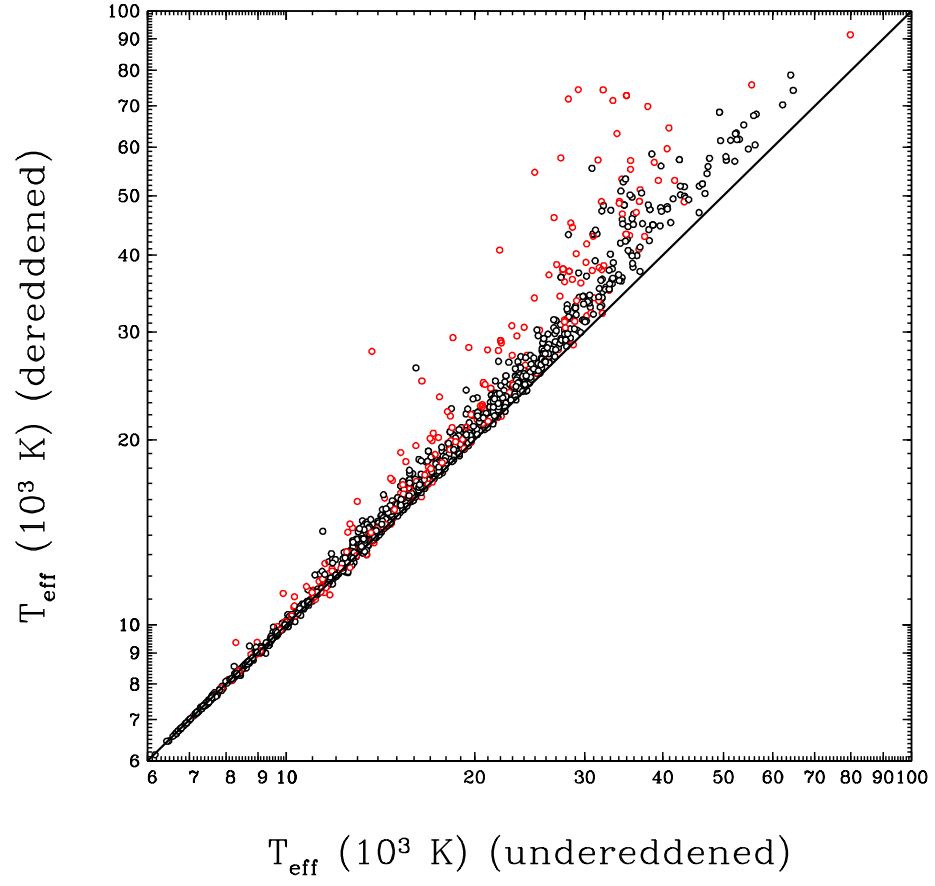


Figure 12

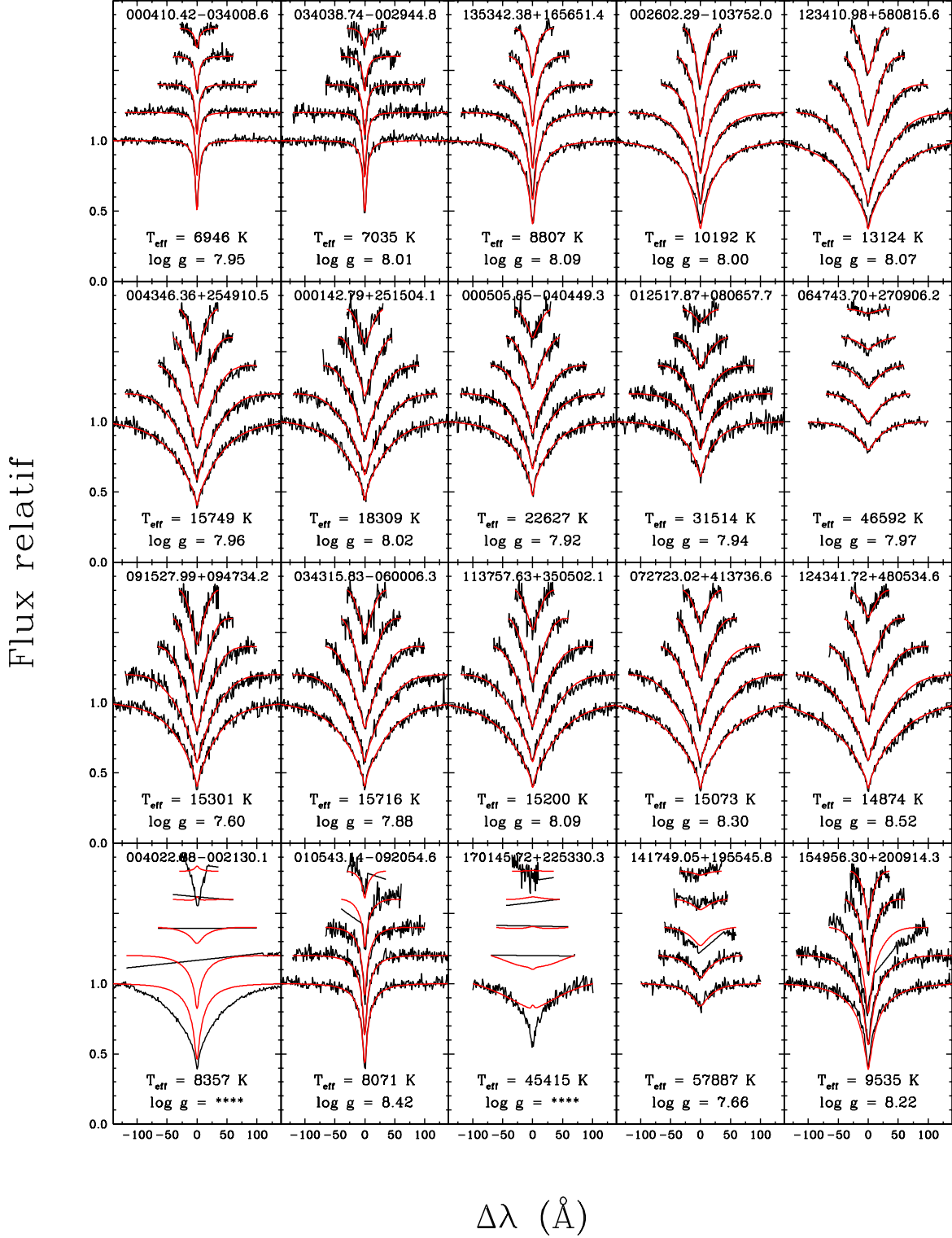


Figure 13



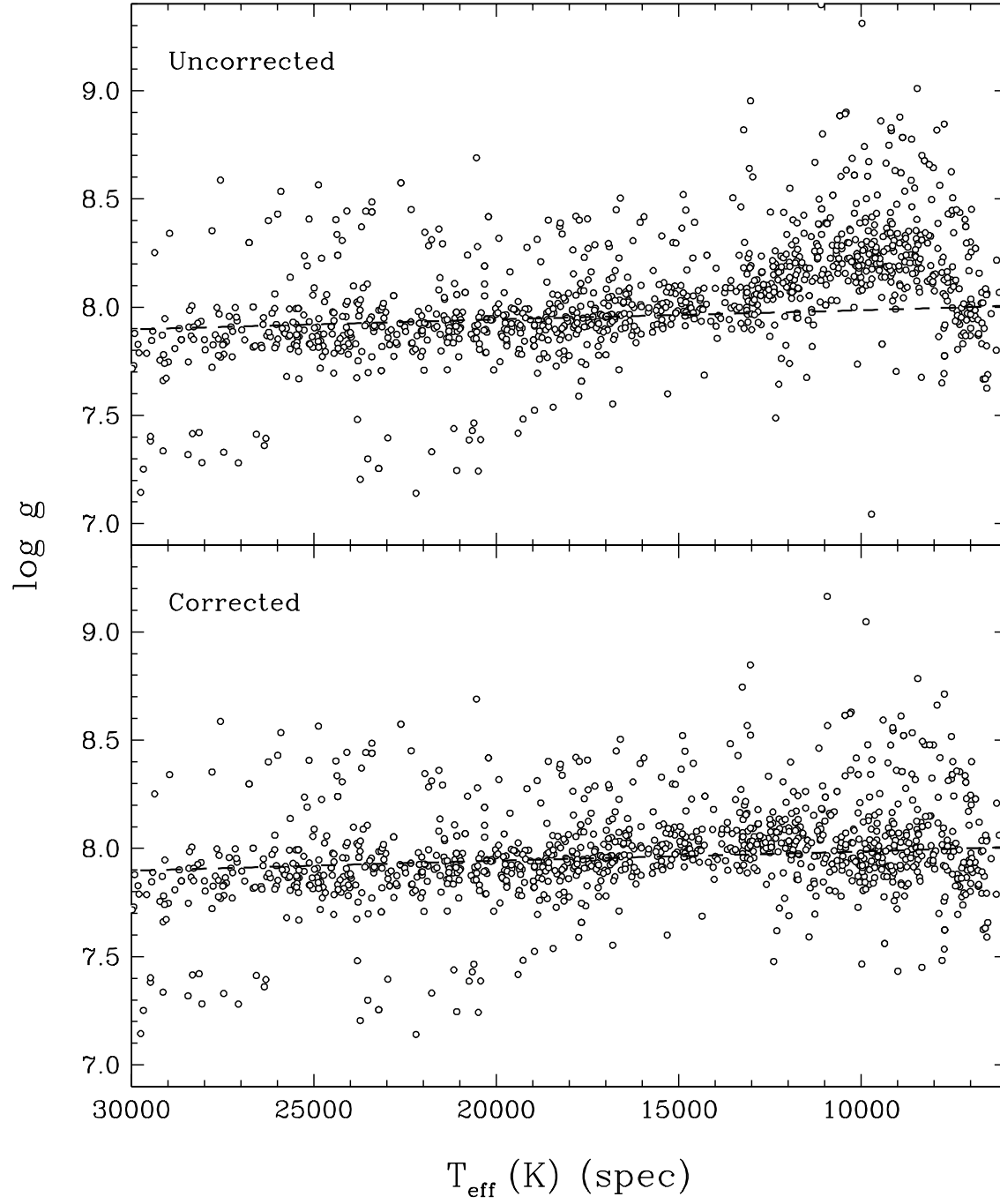


Figure 14

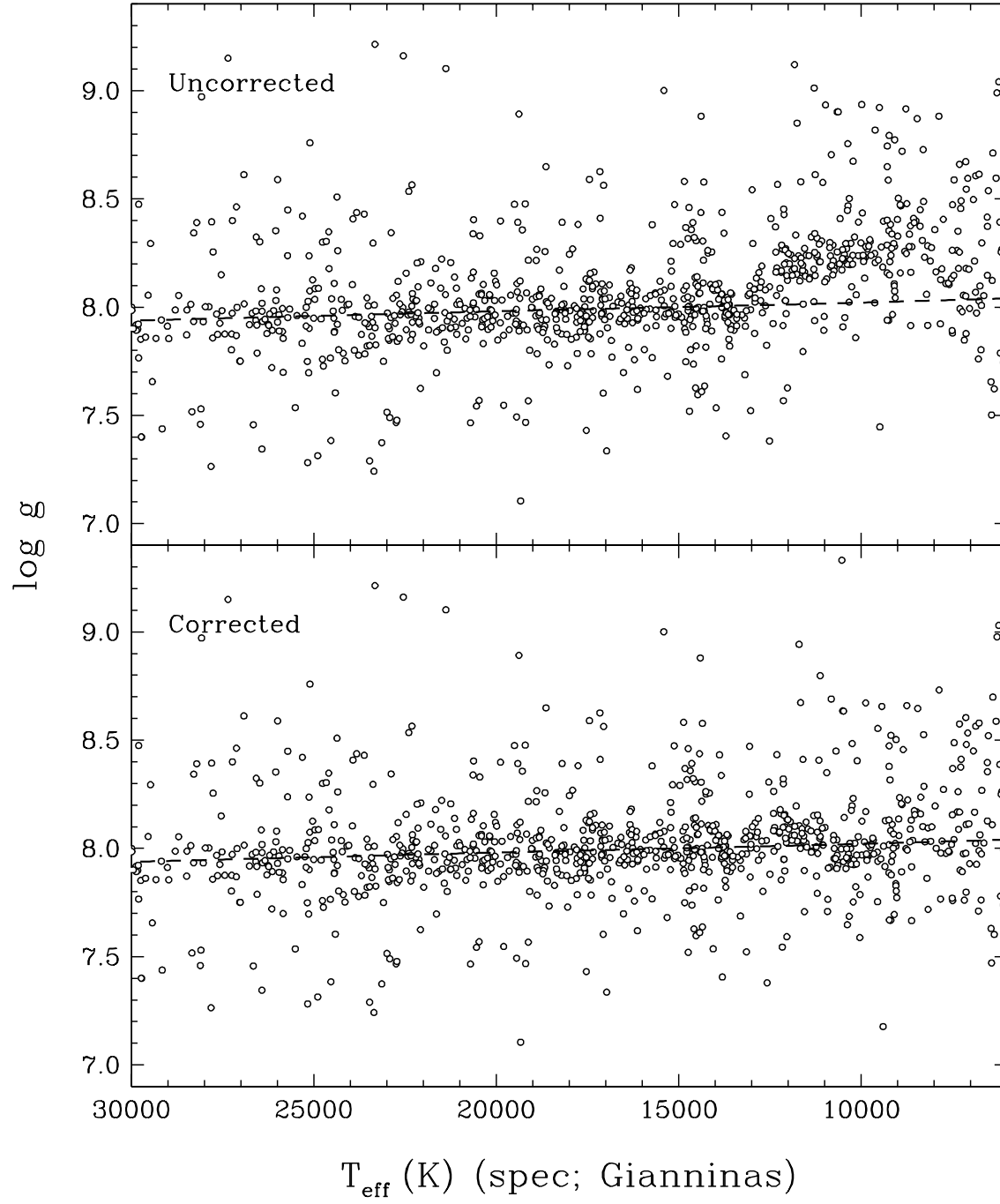


Figure 15

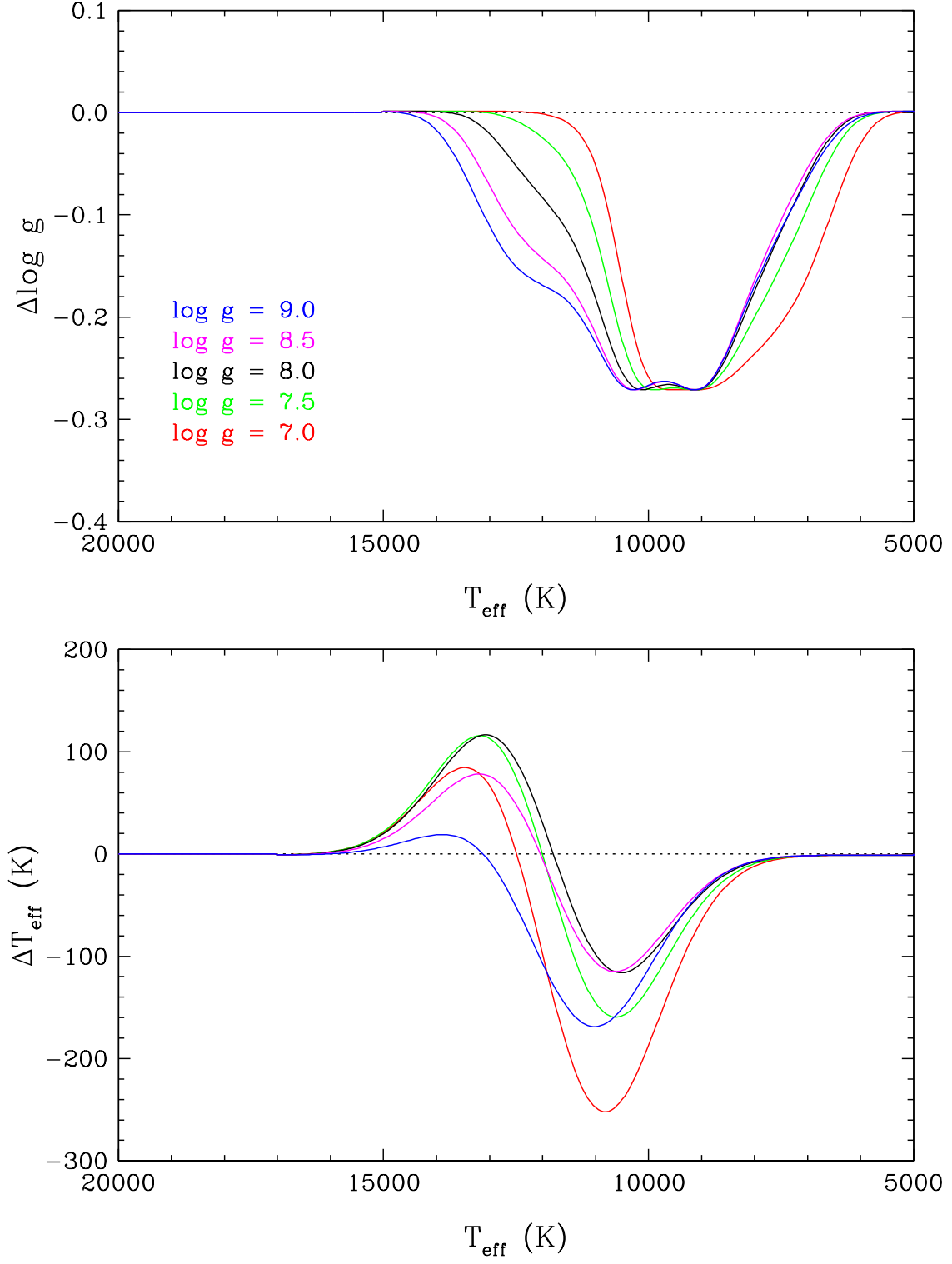


Figure 16

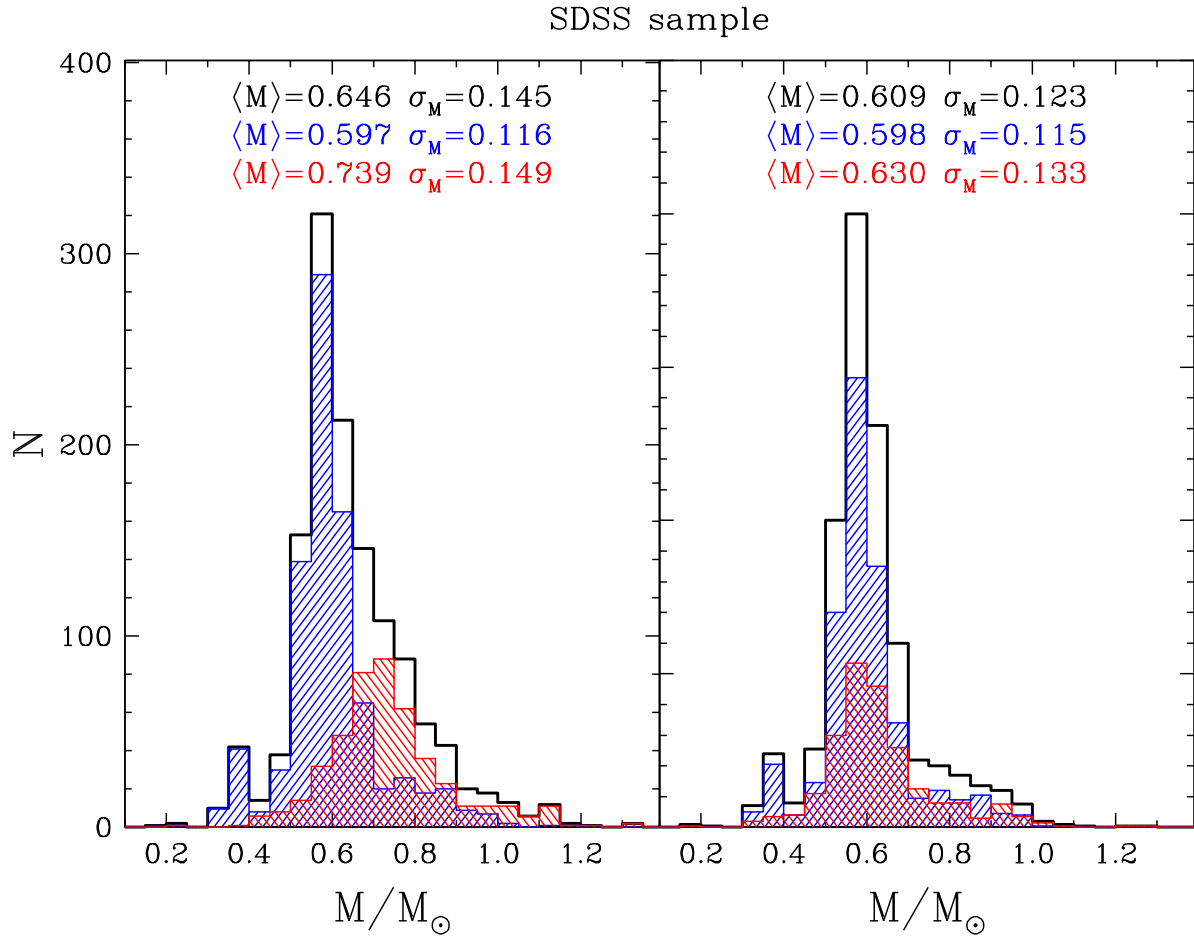


Figure 17

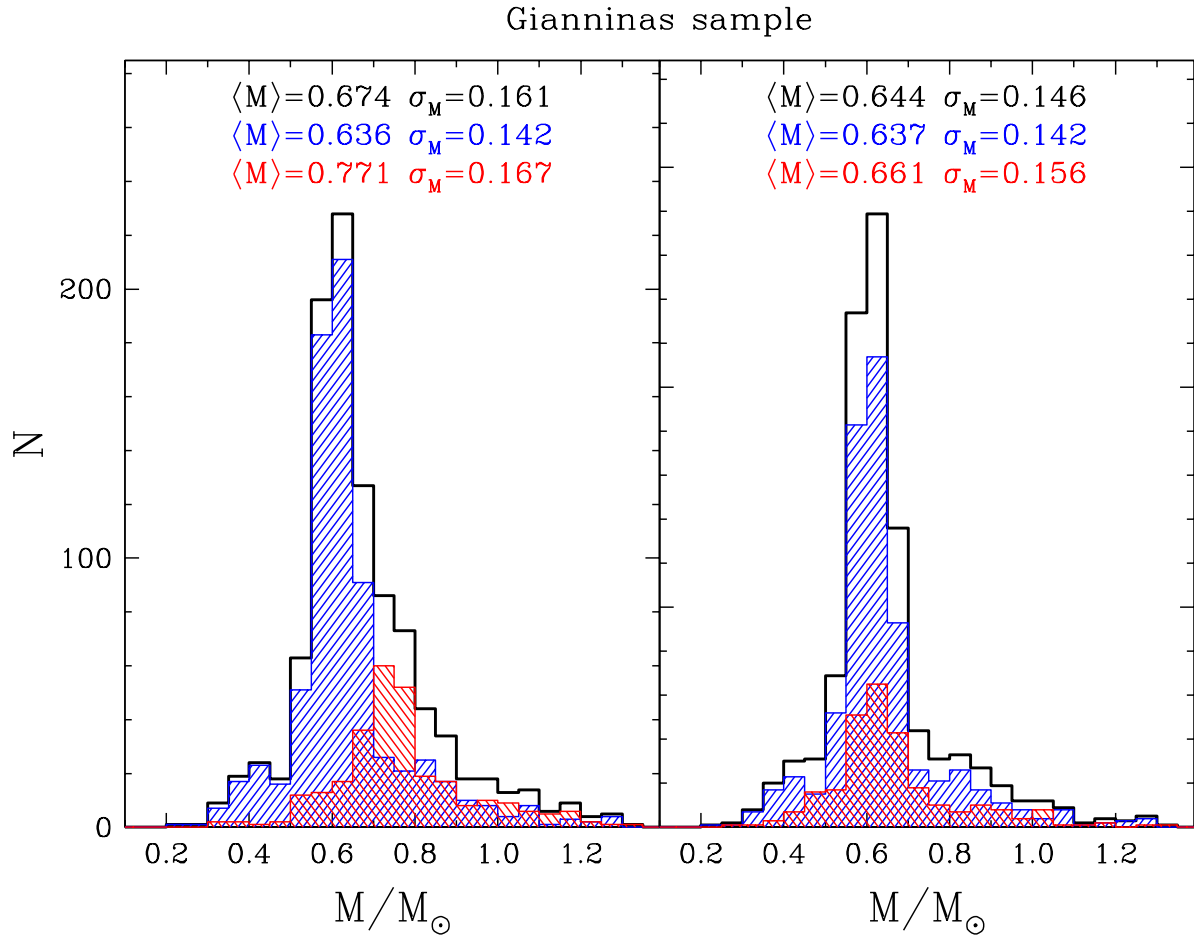


Figure 18

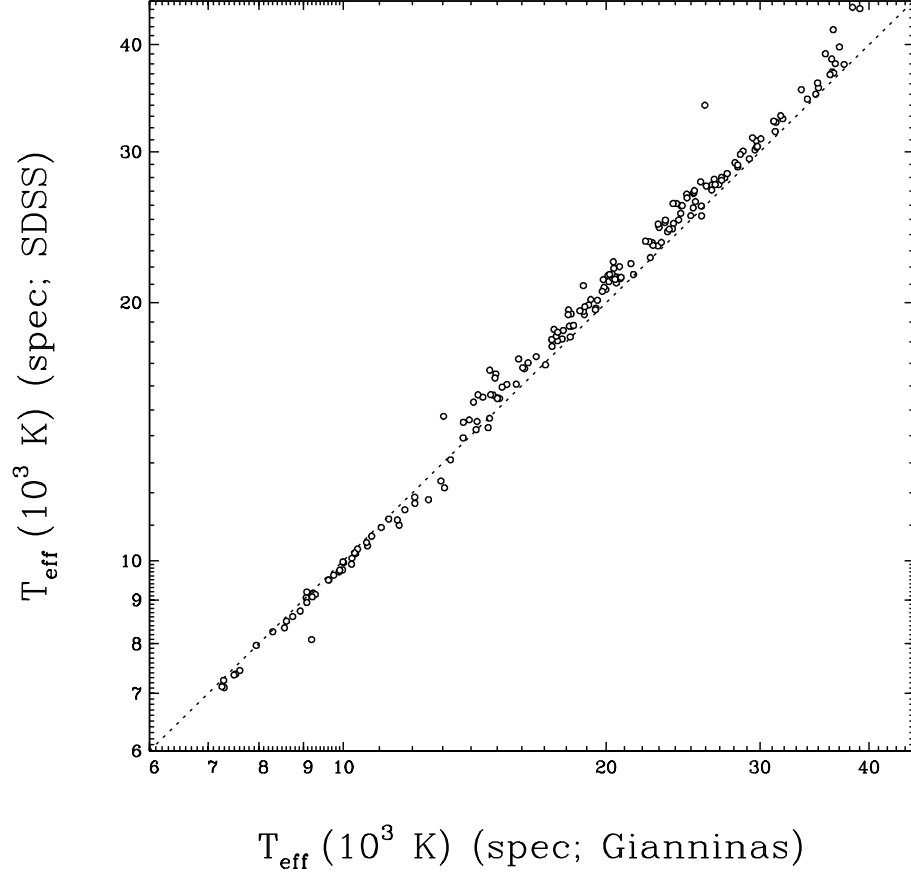


Figure 19

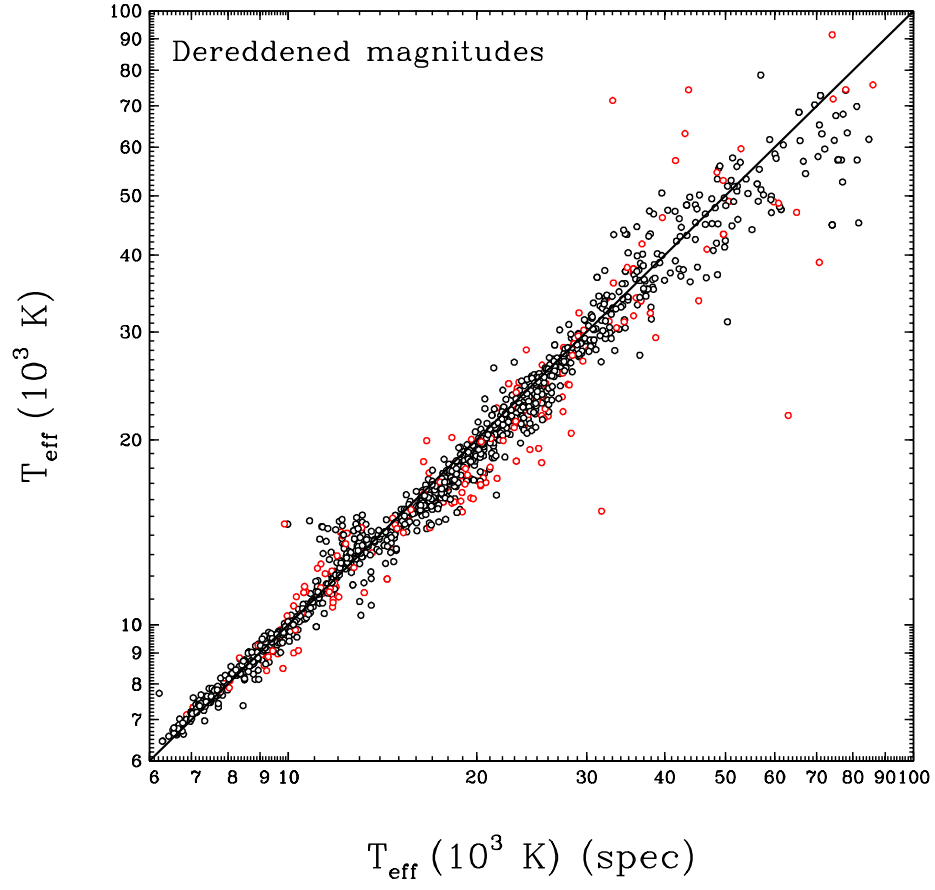


Figure 20

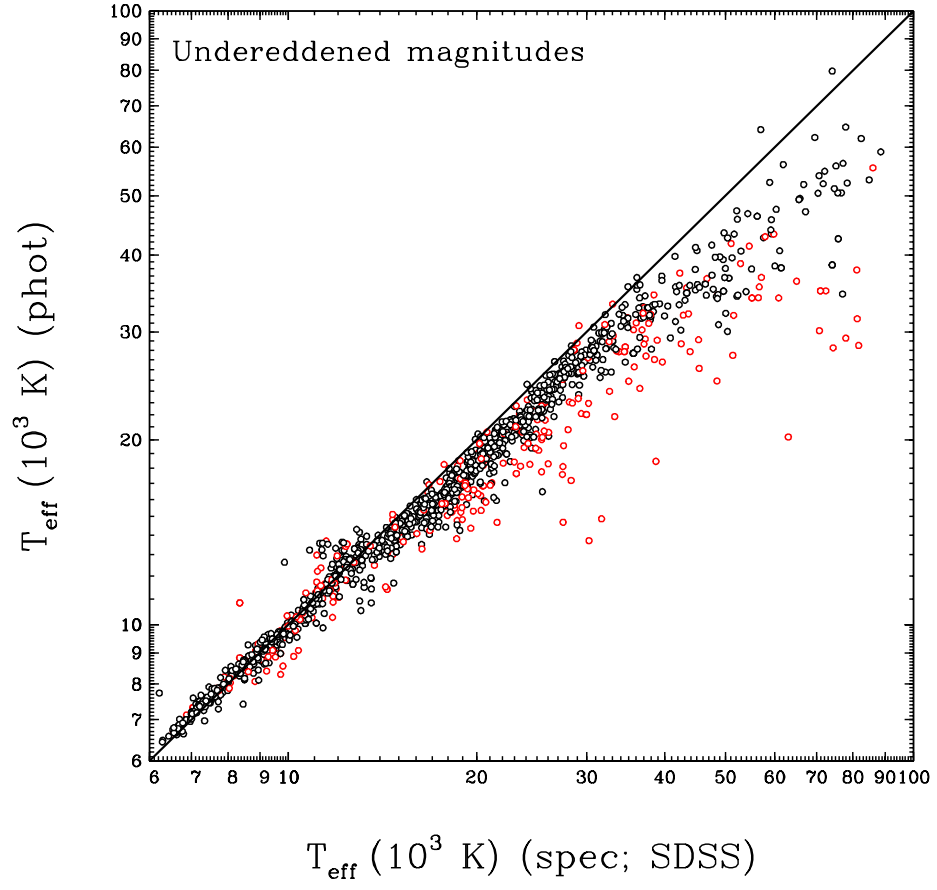


Figure 21



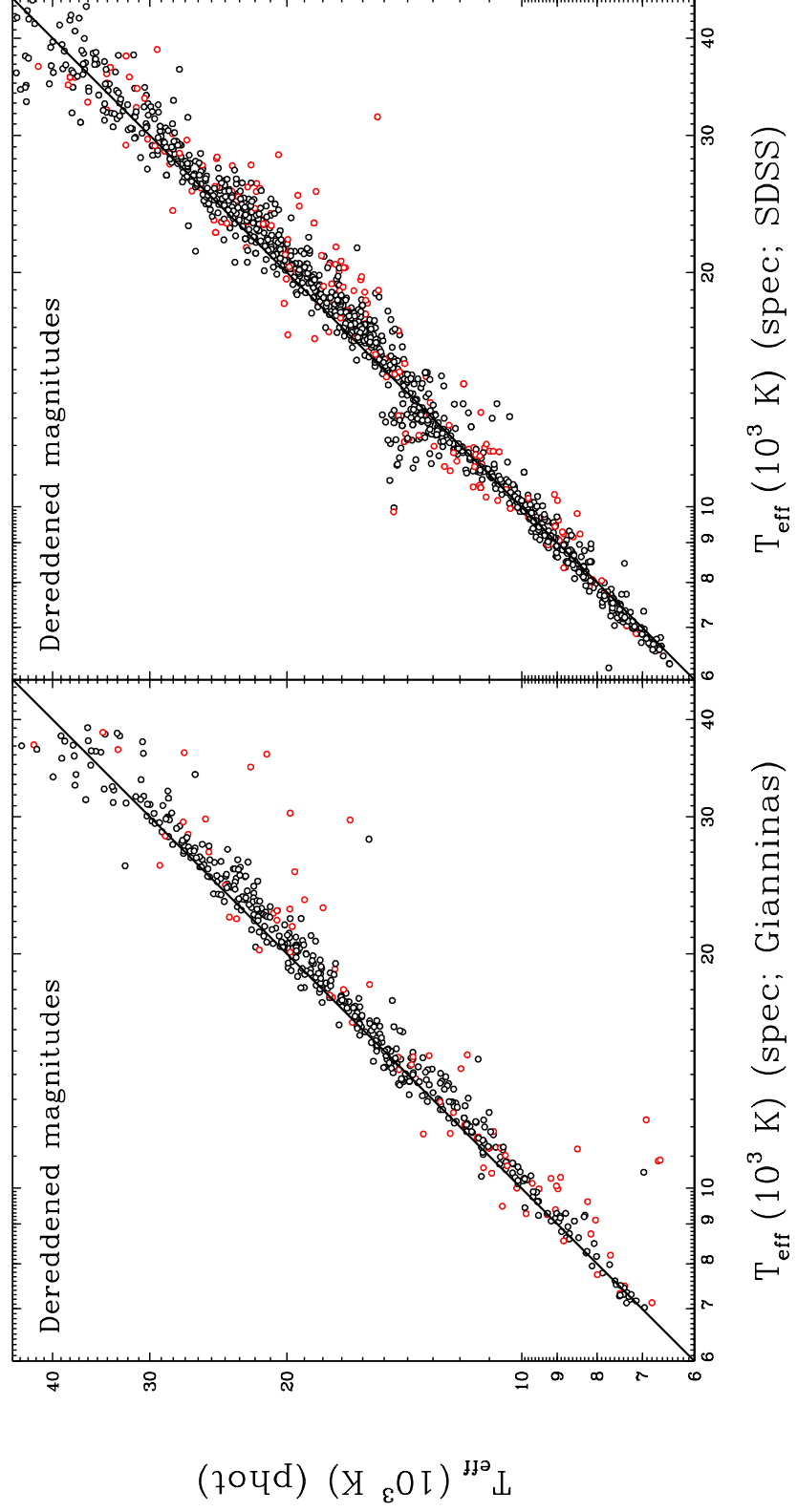


Figure 22

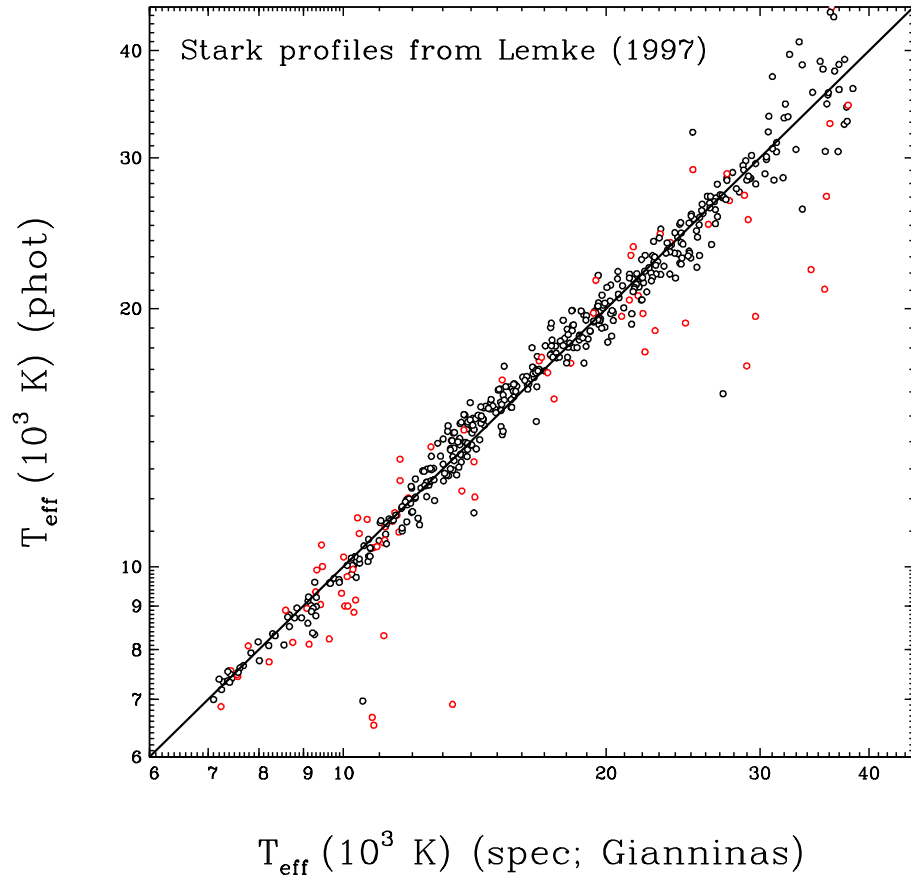


Figure 23

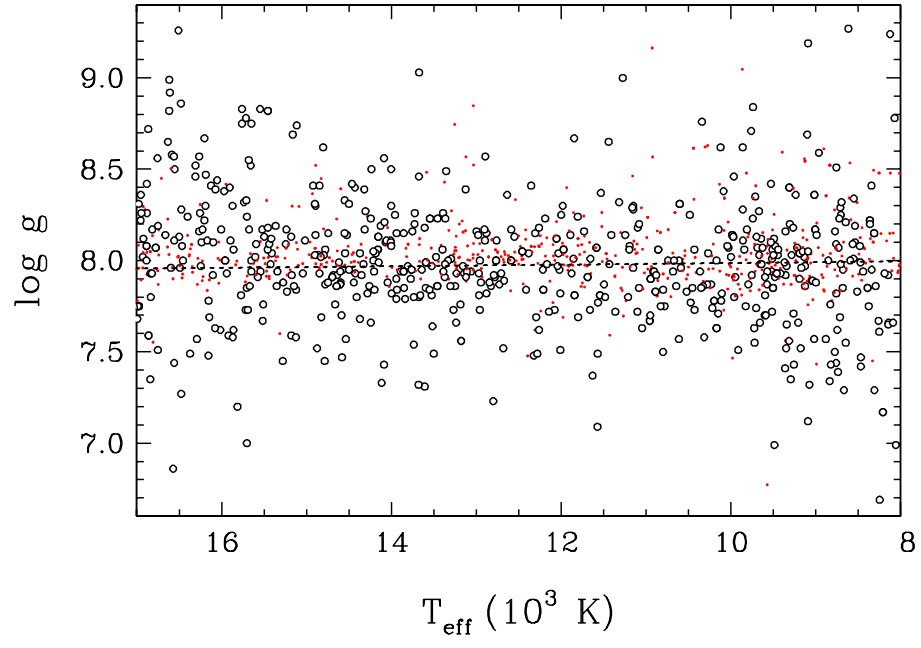


Figure 24

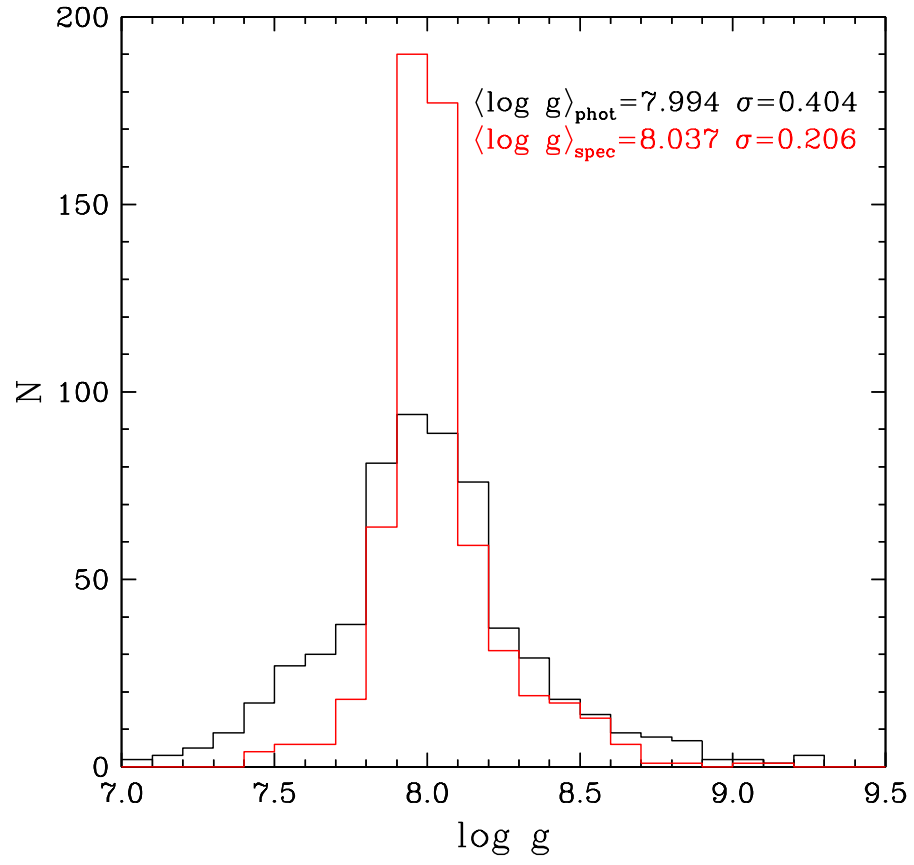


Figure 25